Cell Reports

Report

Modeling spastic paraplegia 4 with corticospinal motor neuron-enriched cortical organoids reveals genotype-phenotype and HDAC6-targetable pathology

Graphical abstract

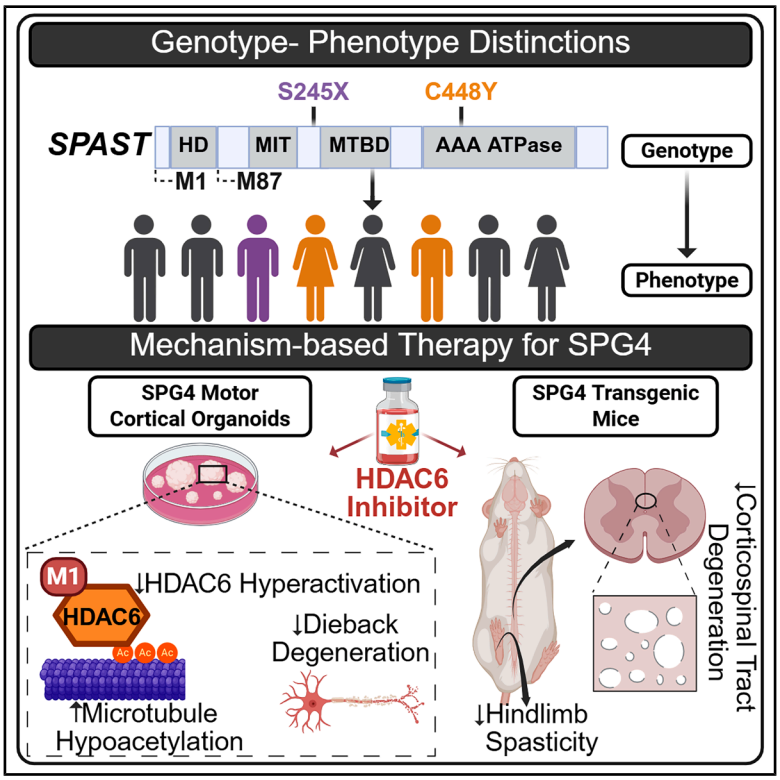

Highlights

- Isogenic hiPSC-derived MCOs reveal potential genotype-phenotype distinctions in SPG4
- Mutant M1-spastin-induced HDAC6 hyperactivation is the key pathogenic culprit
- HDAC6 inhibition restored microtubule acetylation and rescued axonal degeneration in MCOs
- HDAC6 inhibition improves CST integrity and gait deficiency in SPG4 mice

Authors

Neha Mohan, Skandha Ramakrishnan, Xiaohuan Sun, ..., James Cai, Mei Liu, Liang Qiang

Correspondence

liumei@ntu.edu.cn (M.L.), lq24@drexel.edu (L.Q.)

In brief

Mohan et al. generated isogenic hiPSC-derived motor cortical organoids (MCOs) carrying either an SPAST missense or truncation mutation. These models revealed genotype-phenotype distinctions in microtubule defects and axonal degeneration, driven by HDAC6 hyperactivation. Pharmacological inhibition of HDAC6 successfully rescued these pathological phenotypes, establishing HDAC6 as a therapeutic target for SPG4.

Mohan et al., 2026, Cell Reports *45*, 117036
March 24, 2026
https://doi.org/10.1016/j.celrep.2026.117036

CellPress

Cell Reports

CellPress
OPEN ACCESS

Report

Modeling spastic paraplegia 4 with corticospinal motor neuron-enriched cortical organoids reveals genotype-phenotype and HDAC6-targetable pathology

Neha Mohan,[1] Skandha Ramakrishnan,[1] Xiaohuan Sun,[1] Ying Sun,[2] Theresa Connors,[1] Victor Chai,[1] Emanuela Piermarini,[1] Peter W. Baas,[1] James Cai,[3,4,5] Mei Liu,[2,*] and Liang Qiang[1,6,*]

[1]Department of Neurobiology and Anatomy, Drexel University College of Medicine, Philadelphia, PA, USA
[2]Key Laboratory of Neuroregeneration of Jiangsu and Ministry of Education, Co-innovation Center of Neuroregeneration, Nantong University, Nantong, China
[3]Department of Electrical and Computer Engineering, Texas A&M University, College Station, TX 77843, USA
[4]Department of Veterinary Integrative Biosciences, Texas A&M University, College Station, TX 77843, USA
[5]Interdisciplinary Program of Genetics, Texas A&M University, College Station, TX 77843, USA
[6]Lead contact
*Correspondence: liumei@ntu.edu.cn (M.L.), lq24@drexel.edu (L.Q.)
https://doi.org/10.1016/j.celrep.2026.117036

SUMMARY

Spastic paraplegia 4 (SPG4), the most common form of hereditary spastic paraplegia, causes progressive gait deficiency due to corticospinal tract degeneration. SPG4 results from mutations in the *SPAST* gene, which encodes spastin, a microtubule-severing AAA-ATPase. To dissect genotype-phenotype relationships, we generated isogenic human induced pluripotent stem cell lines carrying either an *SPAST* missense ($SPAST^{WT/C448Y}$) or truncation ($SPAST^{WT/S245X}$) mutation and differentiated them into corticospinal motor neuron-enriched cortical organoids. These models revealed mutation-specific patterns of aberrant neuronal activity, microtubule hypoacetylation, and axonal degeneration. We identified mutant M1-spastin-induced hyperactivation of histone deacetylase 6 (HDAC6), a major tubulin deacetylase, as the key pathogenic culprit. Pharmacological inhibition of HDAC6 with tubastatin A restored microtubule acetylation and rescued axonal degeneration in organoids, with corresponding improvements in corticospinal tract integrity and gait defects in SPG4 transgenic mice. Our study uncovers HDAC6 hyperactivation as a targetable mechanism for SPG4 and verifies human organoids as a platform for therapeutic discovery.

INTRODUCTION

Hereditary spastic paraplegia (HSP) is a genetically diverse neurodegenerative disorder characterized by progressive lower limb spasticity and weakness due to degeneration of the corticospinal tract (CST). The CST comprises a bundle of axons that projects from corticospinal motor neurons (CSMNs) in the primary motor cortex.[1–4] Spastic paraplegia 4 (SPG4), caused by mutations in *SPAST*, is the most prevalent autosomal dominant HSP subtype. SPG4 accounts for ~40% of genetically identified cases, with a prevalence of 2–6 per 100,000 individuals.[5,6] Clinically, SPG4 predominantly manifests as pure HSP, although complex forms of HSP exhibit additional features such as ataxia, cognitive impairment, and peripheral neuropathy.[3,7–10] Disease severity and age of onset vary substantially, yet the molecular bases underlying this genotype-phenotype variability remain poorly understood, hindering targetable therapy.[11,12] *SPAST* encodes spastin, an ATPases associated with diverse cellular activities (AAA) family protein important for microtubule dynamics, intracellular organelle function, and neuronal integrity.[13–17] Spastin has two isoforms: the longer ER-targeted M1-spastin, involved in ER morphology and membrane remodeling, and the shorter cytoplasmic M87-spastin, mainly responsible for microtubule severing.[15,18–20] While M87-spastin is more abundant, accumulating evidence suggests mutant M1-spastin significantly drives SPG4 pathology through toxic gain-of-function mechanisms.[21,22] Our prior work suggested that this gain-of-function toxicity can sufficiently lead to neurodegeneration, with *SPAST* haploinsufficiency further exacerbating the pathology.[23,24] However, the isoform-specific contributions to each pathogenic mechanism remain undefined.[20,25] SPAST mutations, encompassing missense, truncation, frameshift, and splice-site variants, uniformly cause axonal degeneration but lead to highly variable clinical presentations.[26] Despite hypothesized roles for genetic modifiers and environmental factors, direct molecular insights into genotype-phenotype distinctions in SPG4 are missing. Emerging studies implicate microtubule hypoacetylation driven by mutant M1-spastin accumulation as a consistent pathological phenotype, regardless of the mutation.[20,23,24,27] Interestingly, histone deacetylase 6 (HDAC6), the primary cytoplasmic tubulin deacetylase in neurons,[28–31] is aberrantly activated in SPG4 transgenic models, though its

pathological relevance in patients with SPG4 remains unverified.[24] Indeed, HDAC6 inhibition has demonstrated therapeutic efficacy in many preclinical models of neurodegenerative diseases such as Alzheimer's disease and amyotrophic lateral sclerosis.[32–36] However, HDAC6 inhibition has not yet been pursued in the context of SPG4. Given the current lack of effective, targeted interventions for SPG4, systematically evaluating HDAC6 inhibition offers a compelling opportunity to address a critical unmet therapeutic need in this disorder.

To address these critical gaps, we established isogenic human induced pluripotent stem cell (hiPSC) lines carrying either a missense ($SPAST^{WT/C448Y}$) or truncation ($SPAST^{WT/S245X}$) mutation introduced via CRISPR-Cas9 editing. These two mutations, representing distinct *SPAST* mutation types observed in patients with SPG4 were generated from the same control line.[37,38] These hiPSCs were differentiated into CSMN-enriched cortical organoids (CSMN-COs) as the 3D human SPG4 model. Combined with validation in our established SPG4-transgenic mice, this novel platform enables precise interrogation of genotype-phenotype distinctions and aims to elucidate HDAC6 hyperactivity as a unifying mechanism and therapeutic target in SPG4.

RESULTS

Derivation of CSMN-enriched COs from isogenic hiPSC lines carrying distinct *SPAST* mutations

To rigorously investigate genotype-phenotype relationships and faithfully recapitulate SPG4 pathology, we generated isogenic hiPSC lines harboring either a missense ($SPAST^{WT/C448Y}$) or a truncation mutation ($SPAST^{WT/S245X}$), each introduced heterozygously into a single parental hiPSC line derived from a healthy 36-year-old male donor, in order to accurately reflect the autosomal dominant inheritance pattern of SPG4. These lines exhibited normal colony morphology, pluripotency expression (Figure 1A), and differentiation capability into all three germ layers (Figure 1B), with confirmed stable male karyotype (Figure 1C). The precise introduction of *SPAST* mutations via CRISPR-Cas9 was validated by targeted PCR and sequencing for both $SPAST^{WT/S245X}$ (Figure 1D) and $SPAST^{WT/C448Y}$ (Figure 1E). CSMN-COs were generated from all three hiPSCs using our optimized protocol, adapted from previously established methods (Figure 1F).[39,40] Briefly, embryoid bodies (EBs) derived from hiPSCs underwent neuronal induction with dual SMAD inhibition, followed by neuronal patterning in the presence of growth factors and the sonic hedgehog (SHH) inhibitor cyclopamine, which is essential for enriching the CSMN population[41,42] followed by neuronal maturation. 1-month-old CSMN-COs from all three hiPSC lines showed robust populations of neural progenitors marked by Sox2 and postmitotic neurons marked by tau and MAP2 (Figures 1G and 1H), with significant neuroepithelial loops resembling active neurogenesis (Figure 1H). Notably, we did not observe any overt differences among the lines in overall neuronal or glial differentiation. At 3 months of differentiation, CSMN-COs exhibited substantial enrichment of CSMNs, as confirmed by prominent expression of established CSMN-specific markers including CTIP2, L1CAM, and vGlut1 (Figures 1I–1M). Importantly, 3-month-old organoids also demonstrated progressive neuronal maturation, characterized by extensive expression of the mature neuronal marker NeuN and the axonal marker phosphorylated neurofilament SMI312. Robust populations of astrocytes exhibiting typical astrocytic morphology and immunoreactivity for GFAP were observed, indicating the establishment of complex neuronal-glial interactions (Figures 1K–1M). By 6 months of differentiation, CSMN-COs displayed dense networks of synapses, as evidenced by widespread expression of synaptophysin (Figure 1N). To further validate functional neuronal activity, we utilized a multi-electrode array (MEA) system, which confirmed spontaneous neuronal firing and network activity within organoids (Figures 1O–1Q). Additionally, single-cell RNA sequencing (scRNA-seq) was performed on 3-month-old healthy hiPSC-derived organoids, resulting in the identification of 4,819 cells expressing a total of 25,052 genes (Figure 2). Unbiased clustering and manual annotation delineated seven distinct cell populations characterized by unique marker gene expression profiles (Figures 2A–2C).[43] Beyond identifying the clusters, we quantified their relative abundance and further resolved cluster-specific expression of CSMN-associated markers (Figures 2B and 2D–2M). Although direct mapping with available datasets was not feasible, our CSMN-COs closely represent heterogeneous cell populations found in the human motor cortex,[44] underscoring the fidelity and physiological relevance of our organoid model; however, some cell types including endothelial cells and microglia are absent from this model. This further highlights the validity and region specificity of our CSMN-COs model. Quantitative qRT-PCR analysis provided further molecular validation of CSMN identity. Compared to conventional forebrain cortical organoids (COs) generated without cyclopamine treatment, our CSMN-COs demonstrated significantly higher expression of the canonical CSMN markers, including CTIP2, L1CAM, CRYM, and vGlut1 (Figures 2N–2S; see Table S2 for mean ± SD).[43,45] Despite prior reports of UCHL1 labeling CSMNs in mice,[46,47] unlike other CSMN markers, our data reveal no difference between pan-cortical and CSMN-COs with regard to UCHL1, aligning with its broad neuronal expression.[48,49]

Distinct genotype-phenotype distinctions in isogenic SPG4 organoids highlight accelerated axonal degeneration and selective CSMN vulnerability in the missense mutation model

SPG4 presents with marked clinical heterogeneity, with mutation type strongly influencing disease onset and progression, suggesting underlying genotype-phenotype distinction.[50] To investigate these differences in our model, we first examined spastin mRNA expression in 6-month-old CSMN-COs using qRT-PCR. Primers targeting both the N-terminal (exons 1–2) and C-terminal (exons 11–12) regions revealed elevated full-length spastin transcripts in both $SPAST^{WT/S245X}$ and $SPAST^{WT/C448Y}$ organoids compared to wild-type controls (Figures 3A and 3B). This was particularly surprising for $SPAST^{WT/S245X}$, which might be expected to undergo nonsense-mediated mRNA decay, yet aligns with previous patient data showing preserved or

CellPress
OPEN ACCESS

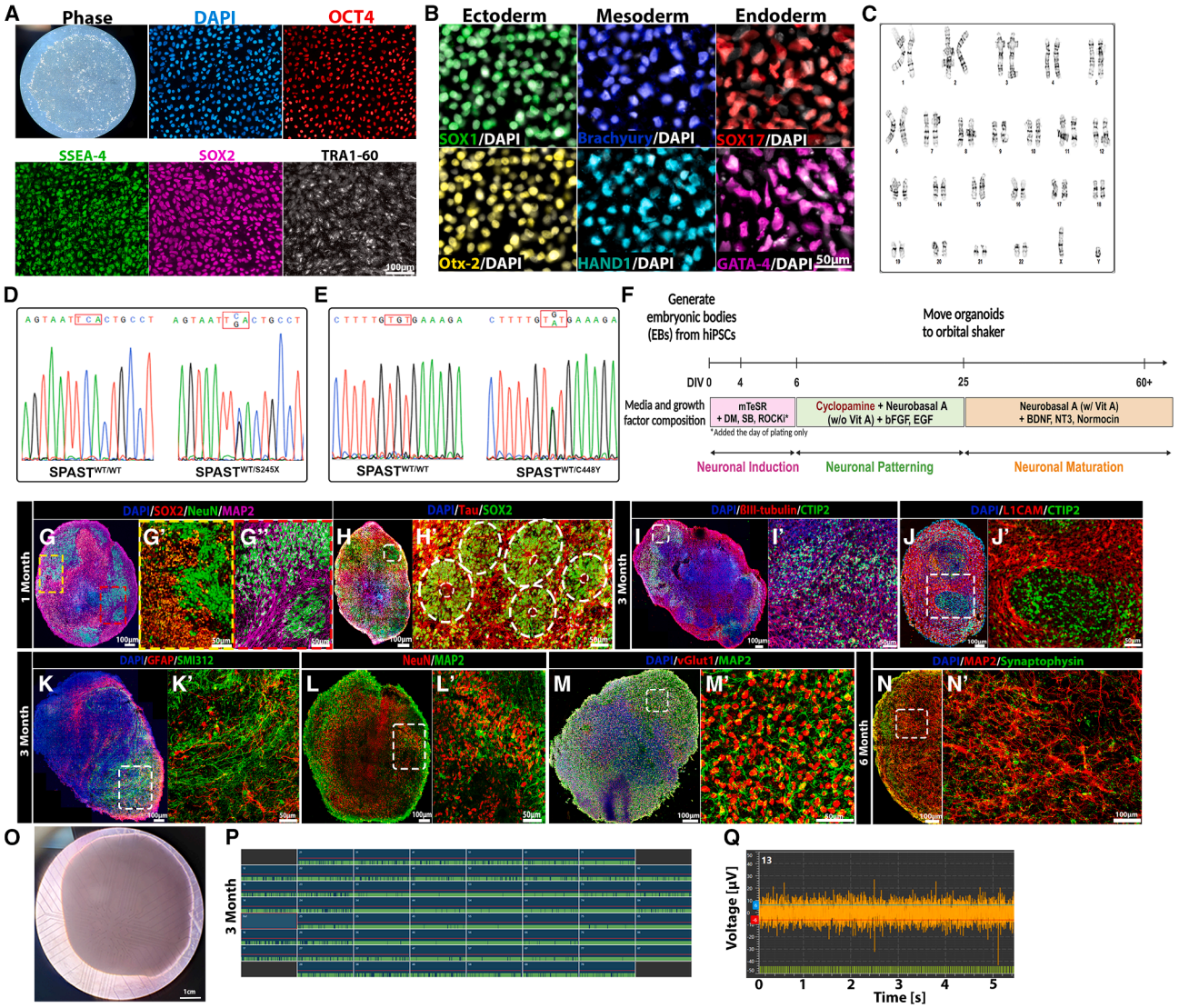

Figure 1. Derivation and characterization of CSMN-COs from isogenic hiPSC lines carrying distinct SPAST mutations

(A) Representative phase-contrast and immunofluorescence images of hiPSC colonies (SPAST$^{WT/WT}$) including DAPI and pluripotent markers OCT4, SSEA-4, SOX2, and TRA-60.

(B) Representative immunofluorescence images for tri-germ layer differentiation of isogenic hiPSCs (SPAST$^{WT/WT}$), including SOX17 and GATA4 (endoderm), Brachyury and HAND1 (mesoderm), and SOX1 and Otx2 (ectoderm).

(C) Normal karyotypes were identified across all three isogenic hiPSC lines, represented by SPAST$^{WT/WT}$.

(D and E) Genomic DNA sequencing confirming the specific genotypes of hiPSC-SPAST$^{WT/S245X}$, hiPSC-SPAST$^{WT/C448Y}$ and hiPSC-SPAST$^{WT/WT}$.

(F) Schematic and timeline of CSMN-CO generation.

(G and H) Representative immunofluorescence images of 1-month CSMN-COs using pan-neuronal (NeuN, Tau, and MAP2) and neural progenitor (SOX2) markers. Dashed circles highlight neuroepithelial loops.

(I–M) Representative immunofluorescence images of 3-month CSMN-COs using pan-neuronal (βIII-tubulin and SMI312), astrocytic (GFAP), and CSMN (CTIP2, L1CAM, and vGlut1) markers.

(N) Representative immunofluorescence images of 6-month CSMN-COs using the presynaptic marker synaptophysin.

(O) Representative phase image of 3-month CSMN-COs docked on a MEA2100 single-well platform.

(P) Representative image showing electrode setup and spontaneous neuronal firing; green lines indicate spike counts, red bars indicate bursts, and blue highlight indicates network burst.

(Q) Raster plot from (P) showing individual spikes from electrode number 13 with a standard deviation of ±6 from baseline recording (+6: blue line, and −6: red line).

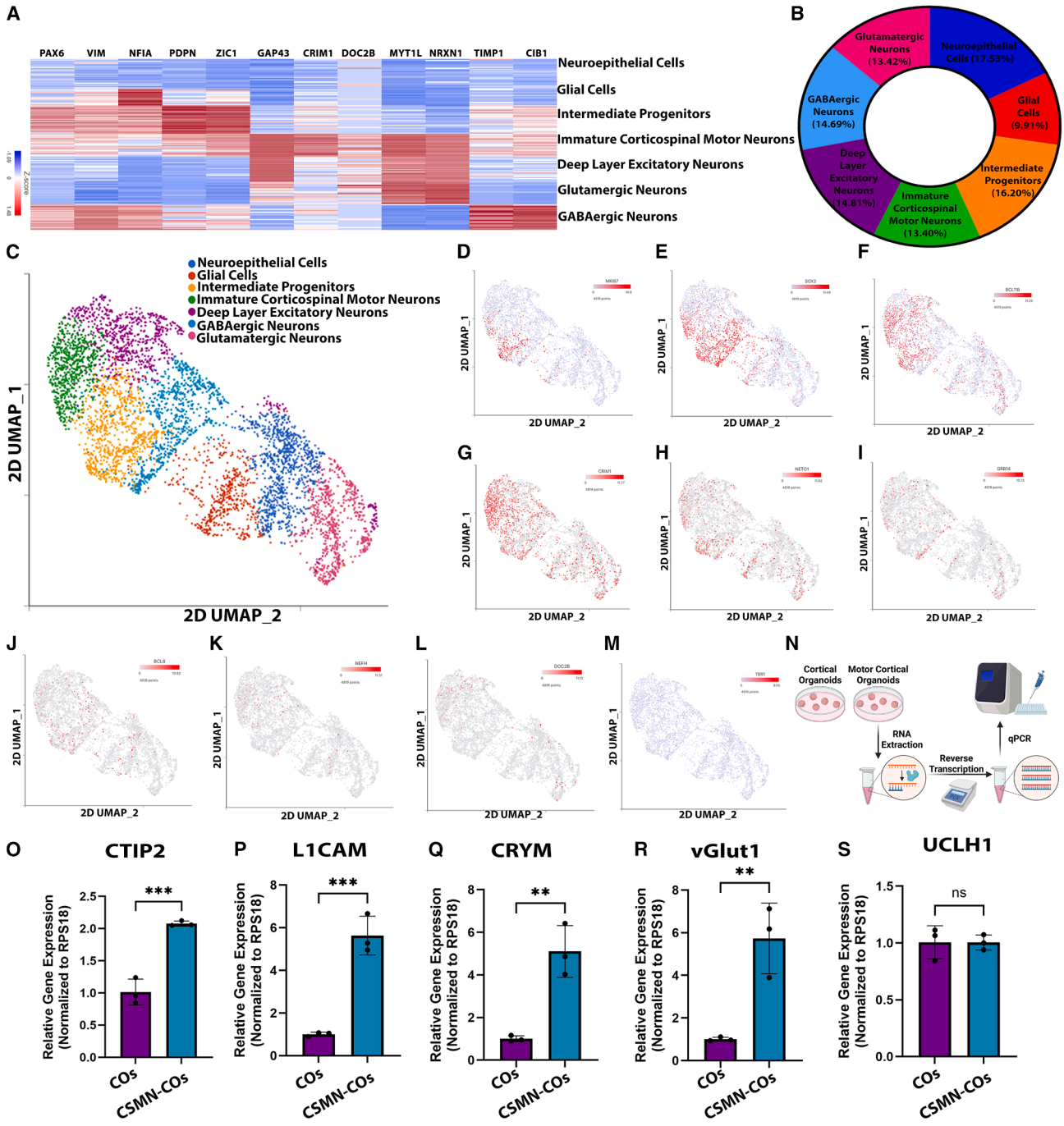

Figure 2. Single-cell RNA sequencing-based characterization and comparative analysis of CSMN-COs

(A) Heatmap representation of cell-type-specific marker genes of scRNA-seq of 3-month-old CSMN-COs: neuroepithelial cells, glial cells, intermediate progenitors, corticospinal motor neurons, deep layer excitatory neurons, GABAergic neurons, and glutamatergic neurons (see Supplementary file for details).

(B) Pie chart representation of cell-type proportions within the CSMN-COs.

(C–M) 2D UMAP plot representing the annotated clusters (C). Expression of selected markers associated with lineage of intermediate progenitors and corticospinal motor neurons (D–M).

(N–S) Experimental design and qRT-PCR analysis of CSMN-specific genes, normalized to RSP18 in 6-month generic cortical organoids (COs) ($n = 3$) vs. CSMN-COs ($n = 3$).

Unpaired t test. $^{**}p < 0.05$, $^{***}p < 0.001$. All data shown as mean ± SD; see Table S1 for details.

CellPress
OPEN ACCESS

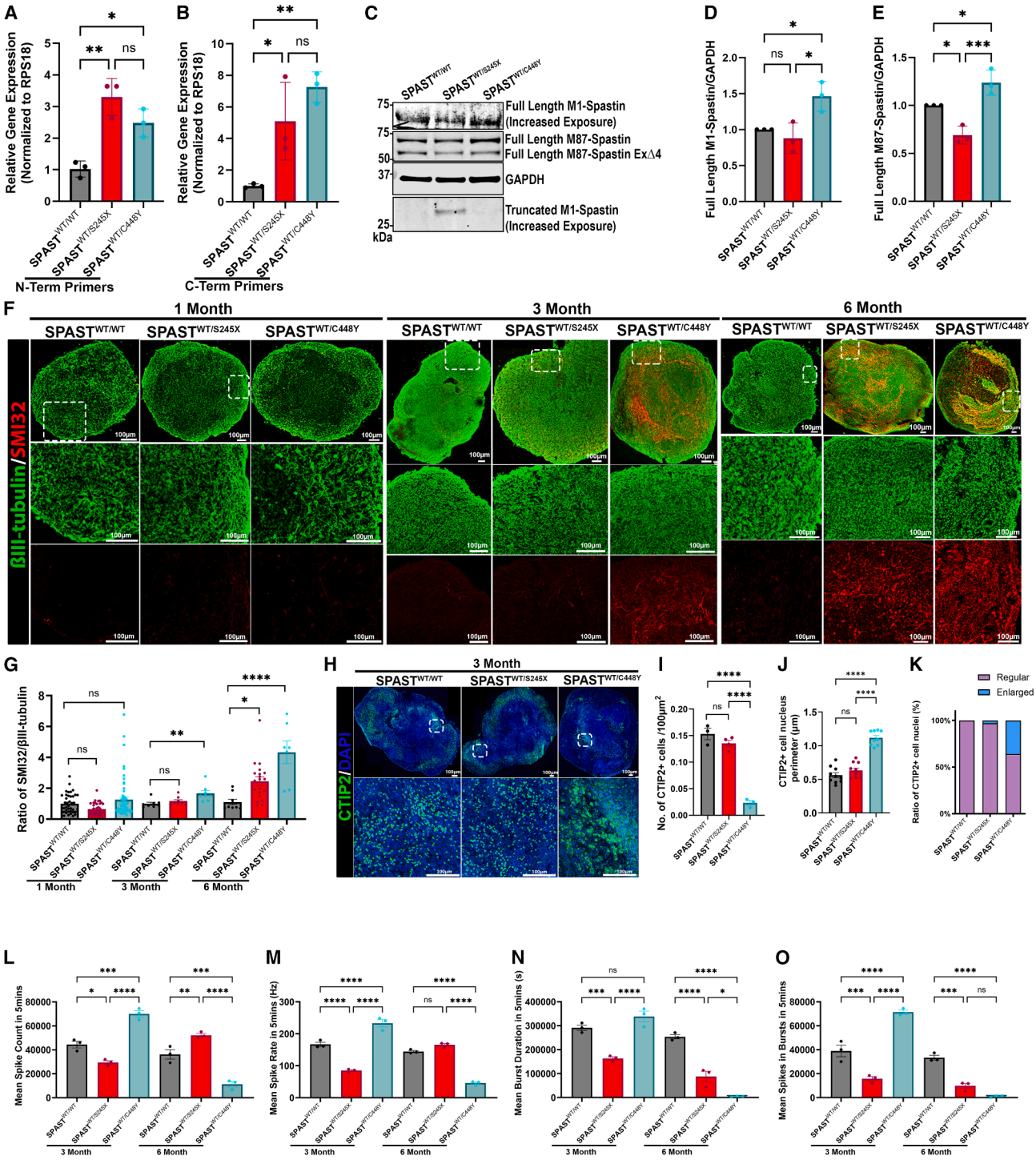

Figure 3. Genotype-phenotype distinctions in isogenic SPG4 CSMN-COs highlight accelerated axonal degeneration and selective CSMN vulnerability in SPAST$^{WT/C448Y}$

(A and B) Characterization of spastin expression in 6-month CSMN-COs derived from the three isogenic genotypes (n = 3 organoids), normalized to RSP18 revealed by qRT-PCR with N-terminal primers (A) and C-terminal primers (B).

(C–E) Representative western blot (WB) of spastin in 6-month-old MC organoids (C, n = 3). Levels of full-length M1-spastin (D) and M87-spastin (E) in SPAST$^{WT/S245X}$ and SPAST$^{WT/C448Y}$, both normalized to GAPDH relative to SPAST$^{WT/WT}$. Note that a truncated product of SPAST$^{WT/S245X}$ CSMN-COs has been identified with predicted molecular weight.

(legend continued on next page)

elevated *SPAST* mRNA levels despite truncating mutations.[51] No significant difference was observed between the two mutant groups at the transcript level. At the protein level, SPAST$^{WT/S245X}$ organoids showed modest reduction in full-length M1- and M87-spastin, whereas SPAST$^{WT/C448Y}$ organoids displayed increased levels of both isoforms (Figures 3C–3E). Notably, a truncated M1 spastin species was detected in the SPAST$^{WT/S245X}$ organoids, reinforcing the possibility that aberrant accumulation of mutant protein may confer gain-of-function toxicity in SPG4 truncation mutants.

Given prior clinical findings linking AAA domain missense mutations to earlier onset and more severe SPG4 phenotypes[26,50,52] than the truncation mutations, we next sought to determine whether our model recapitulates these differential degenerative trajectories. We performed a temporal analysis of axonal degeneration using SMI32, a dephosphorylated neurofilament marker of axonal degeneration.[53,54] At 1 month, neither mutant showed signs of axonal degeneration. However, by 3 months, SPAST$^{WT/C448Y}$ organoids exhibited a significant increase in SMI32 signal, which intensified by 6 months (Figure 3F). In contrast, SPAST$^{WT/S245X}$ organoids only showed enhanced SMI32 at the 6-month time point (Figures 3F and 3G), suggesting a delayed degenerative course. Corroborating the axonal degeneration phenotype, we observed a marked reduction in CSMNs, identified by the expression of CTIP2, in 3-month-old SPAST$^{WT/C448Y}$ organoids compared to isogenic wild-type controls (Figures 3H and 3I). In SPAST$^{WT/C448Y}$ organoids, we observed a subset of CTIP2^{+} neurons exhibiting markedly enlarged and morphologically disrupted nuclei, confirmed by colocalization with DAPI, consistent with early apoptotic changes rather than cytoplasmic mislocalization of CTIP2. (Figure 3J).[55–58] This nuclear enlargement phenotype was specific to CTIP2^{+} neurons, most prominent in SPAST$^{WT/C448Y}$, less frequent in SPAST$^{WT/S245X}$, and absent in SPAST$^{WT/WT}$ organoids (Figure 3K). Notably, these phenotypes, including CSMN loss and somatic hypertrophy, were absent in SPAST$^{WT/S245X}$ organoids, further underscoring the mutation-specific nature of the SPG4 neurodegenerative progression. To further dissect the genotype-phenotype differences, we employed electrophysiological recordings using a single-well MEA platform to record extracellular neuronal activity in mature CSMN-COs. 3-month-old SPAST$^{WT/C448Y}$ CSMN-COs displayed neuronal hyperactivity denoted by increased spike count and rate (Figures 3K–3L), along with increased burst duration and number of spikes in bursts (Figures 3M and 3N), whereas the SPAST$^{WT/S245X}$ CSMN-COs demonstrated reduced neuronal activity. Subsequently, at 6 months, SPAST$^{WT/C448Y}$ CSMN-COs exhibit diminished neuronal activity, with the SPAST$^{WT/S245X}$ CSMN-COs following suit for burst duration and number of spikes in bursts; however, spike count and rate show neuronal hyperactivity (Figures 3K–3N; see Table S3 for mean ± SD). This bi-phasic change in neuronal activity coincides with progressive axonal degeneration. These data reveal that our novel CSMN enriched cortical organoids recapitulate key genotype-phenotype features of SPG4, including the earlier and more severe neuronal pathology associated with AAA domain missense mutations.

Differential yet convergent HDAC6 hyperactivation induced microtubule hypoacetylation underlies the axonal degeneration in distinct *SPAST*-mutant organoids

Given the distinct yet partially overlapping neurodegenerative phenotypes observed in SPAST$^{WT/C448Y}$ and SPAST$^{WT/S245X}$ CSMN-COs, we next investigated whether these mutation-specific outcomes converge on shared downstream mechanisms. We focused on dysregulation of microtubule acetylation, previously implicated as a key pathological feature in SPG4 models.[23,24] While aberrant HDAC6 activation-induced microtubule hypoacetylation was identified in one SPG4 mouse model,[24] its relevance across diverse *SPAST* mutations remains unclear. Thus, we examined microtubule acetylation and the corresponding HDAC6 activity at different time points in our mutant organoids. At 3 months, SPAST$^{WT/C448Y}$ organoids exhibited a marked reduction in microtubule acetylation and elevated HDAC6 activity, while SPAST$^{WT/S245X}$ organoids retained near-normal levels of both (Figures 4A, 4B, and 4G). By 6 months, however, both mutant lines displayed significant microtubule hypoacetylation and HDAC6 hyperactivation, further highlighting delayed pathological onset in SPAST$^{WT/S245X}$ (Figures 4A–4C and 4H). Importantly, these changes in HDAC6 activity occurred without alterations in total HDAC6 protein levels (Figures 4I and 4J), suggesting possible posttranslational dysregulation. This temporal divergence in HDAC6-microtubule defects mirrors the genotype-specific pattern of axonal degeneration, reinforcing a mechanistic link between HDAC6 activation and neurodegenerative progression in SPG4.

To evaluate the therapeutic potential of targeting HDAC6, we treated organoids with tubastatin A (Tub A), a selective HDAC6 inhibitor. We evaluated the optimal dose of Tub A treatment in organoids in a dose dependent manner (data not shown), in conjunction with previously published studies.[59–63] A 100 μM Tub A treatment successfully suppressed HDAC6 hyperactivity and normalized microtubule acetylation in both genotypes at their respective stages of pathology (Figures 4A–4C and 4G–4H). Interestingly, Tub A significantly reduced SMI32 accumulation and improved

(F and G) Representative immunofluorescence images of 1-, 3-, and 6-month CSMN-COs from all three genotypes marked by SMI32, the early axonal degeneration marker (F), normalized to βIII-tubulin and quantified (G).

(H–K) Representative immunofluorescence images of CSMN populations marked by CTIP2 in 3-month CSMN-COs from all three genotypes (H, $n = 3$) and quantification analyses of the numbers (I) and cell nucleus perimeters (J) of CTIP2^{+} cells. Stacked bar graph showing the percentage of CTIP2+ cell nuclei for all genotypes comparing the ratio of regular and enlarged nuclei. SPAST$^{WT/WT}$ contains 100% regular nuclei, SPAST$^{WT/S245X}$ contains 97.01% regular and 2.98% enlarged nuclei, and lastly, SPAST$^{WT/C448Y}$ contains 64.21% regular and 35.79% enlarged nuclei. $n = 200$ cells from 3 organoids per genotype (K).

(K–N) Spontaneous extracellular neuronal activity over 5-min recording of 3- and 6-month CSMN-COs from all three genotypes ($n = 3$). The graphs show mean spike count that passed the threshold (K), mean spike rate (L), mean burst duration that surpasses a minimum of 50 milliseconds (ms) (M), and mean number of spikes to be considered a burst (N).

One-way ANOVA with Tukey *post hoc* analysis. $^{*}p < 0.05$, $^{**}p < 0.005$, $^{***}p < 0.001$, $^{****}p < 0.0001$. All data shown as mean ± SD; see Table S2 for details.

CellPress
OPEN ACCESS

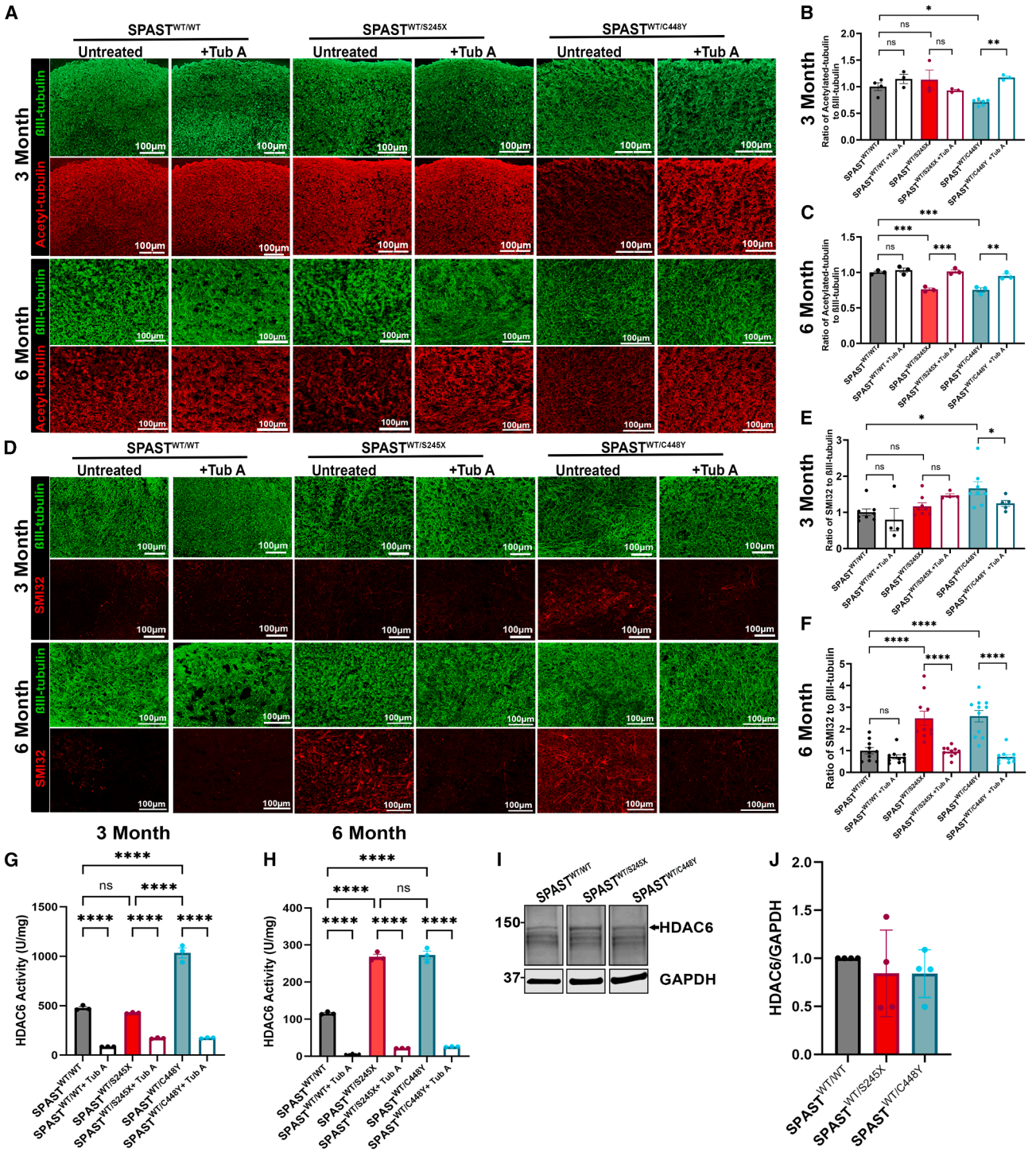

Figure 4. HDAC6 hyperactivation induced by mutant M1-spastin drives microtubule hypoacetylation and axonal degeneration in SPAST-mutant CSMN-COs

(A) Representative immunofluorescence images of 3- and 6-month CSMN-COs derived from SPAST$^{WT/WT}$, SPAST$^{WT/S245X}$, and SPAST$^{WT/C448Y}$ lines, untreated or treated with the HDAC6 inhibitor Tub A, stained for acetylated tubulin and βIII-tubulin.

(B and C) Quantification of the acetylated tubulin-to-βIII-tubulin ratio in 3-month (B) and 6-month (C) CSMN-COs (n = 3–6). Tub A significantly increased tubulin acetylation in mutant CSMN-COs.

(D) Representative immunofluorescence images of 3- and 6-month-old CSMN-COs from SPAST$^{WT/WT}$, SPAST$^{WT/S245X}$, and SPAST$^{WT/C448Y}$ lines, untreated or treated with Tub A, and stained for SMI32 (a marker of early axonal degeneration) and βIII-tubulin.

(legend continued on next page)

axonal morphology, indicating structural rescue of degeneration (Figures 4D–4F; see Tables S4 and S5 for mean ± SD). These findings establish HDAC6 hyperactivation and microtubule hypoacetylation as temporally distinct yet converging mechanisms in SPG4 pathogenesis, driven by mutation-specific dynamics. Moreover, they validate HDAC6 inhibition as a mechanistically grounded, genotype-spanning therapeutic strategy.

HDAC6 selectively interacts with M1-spastin and is aberrantly activated by mutant forms

Given that both SPAST$^{WT/S245X}$ and SPAST$^{WT/C448Y}$ organoids exhibit HDAC6 hyperactivation and microtubule hypoacetylation, in addition to our previous findings that mutant M1-spastin rather than M87-spastin, irrespective of mutation type, consistently drives this phenotype, next, we sought to determine whether these effects arise from a direct, isoform-specific interaction between spastin and HDAC6. Co-immunoprecipitation (coIP) assays in HEK293T cells expressing mCherry-tagged HDAC6 and Flag-tagged spastin isoforms revealed robust interaction between HDAC6 and all M1 variants (WT, C448Y, S245X), whereas no interaction was observed with wild-type M87-spastin (Figures 5A and 5B). Additionally, coIP examination using anti-Flag beads further confirmed this M1-specific association with endogenous HDAC6 (Figures 5C and 5D). Quantitative analyses revealed that both M1-SPAST^{S245X} and M1-SPAST^{C448Y} exhibited increased HDAC6 binding relative to wild-type, with M1-SPAST^{C448Y} showing the highest level of interaction (Figure 5E). Moreover, HDAC6 co-immunoprecipitated with M1-SPAST^{C448Y} displayed significantly elevated phosphorylation, as detected by a phospho-HDAC6-specific antibody, suggesting enhanced enzymatic activation compared to wild-type and truncation variants (Figures 5C and 5E). To further validate this observation, we performed HDAC6 siRNA knockdown in an HEK293T cell line overexpressing M1-C448Y spastin and observed rescue of α-tubulin hypoacetylation (Figures 5F and 5G). To determine whether HDAC6 hyperactivation is a shared downstream effector of mutant spastin toxicity and whether this effect is isoform specific, we quantified HDAC6 enzymatic activity in SH-SY5Y cells expressing wild-type or mutant M1- or M87-spastin.[22] HDAC6 activity remained unaltered in cells expressing either wild-type M1-spastin or any form of M87-spastin. In contrast, all mutant M1-spastins markedly increased HDAC6 activity, regardless of mutation type (Figure 5E; see Tables S6 and S7 for mean ± SD). These findings implicate mutant M1-spastin, irrespective of mutation type, as a key driver of HDAC6 hyperactivation and support a convergent pathological mechanism underlying SPG4.

Pharmacological inhibition of HDAC6 ameliorates gait deficiency and CST degeneration in SPG4-transgenic mice

To validate our organoid-based findings *in vivo*, we employed a novel double heterozygous (dHet) SPG4-transgenic mouse model (hSPAST-C448Y$^{+/-}$; m*Spast*$^{-/+}$), which harbors one allele of the SPAST^{C448Y} mutation, the same as our missense mutant hiPSC line, and one null allele of endogenous mouse *Spast*. This recently developed mouse model recapitulates some key aspects of human SPG4 by combining gain-of-function toxicity and haploinsufficiency, exhibiting pathological phenotypes including progressive gait impairment, CST degeneration, and axonal swelling.[24] Consistent with our organoid data, dHet mice also exhibit reduced microtubule acetylation and aberrant HDAC6 hyperactivation.[24] We treated 3-month-old male dHet mice, corresponding to symptom onset, with Tub A via daily intraperitoneal injection for 21 days (Figure 6A). Serum chemistry confirmed no hepatotoxicity, indicating favorable tolerability (Table S8). Gait analysis using the CatWalk XT system revealed significant hindlimb deficits in dHet mice, including decreased print width, length, area, and altered paw placement, consistent with motor phenotypes reported in individuals with SPG4 which were significantly ameliorated following Tub A treatment (Figures 6B–6F). As expected, no forelimb differences were detected, in line with previous observations.[24] Furthermore, Tub A effectively suppressed hyperactivated HDAC6 and restored microtubule acetylation without altering overall neuronal microtubule mass (Figures 6G–6J). Anatomical evaluation of CST axons via toluidine blue staining of semi-thin spinal cord sections revealed reduced axonal density and increased swelling in the ventral portion of the lumbar dorsal column of dHet mice, as previously reported,[24] which were partially rescued by Tub A treatment (Figures 6K–6N; see Table S9 for mean ± SD). No significant changes were detected at the cervical level. Together, these *in vivo* results substantiate HDAC6 hyperactivation as a disease-relevant, therapeutically modifiable mechanism in SPG4. The convergence between organoid and animal model findings strongly supports selective HDAC6 inhibition as a viable strategy for mitigating CST degeneration and motor deficits in patients with SPG4.

DISCUSSION

Our study establishes an innovative, physiologically relevant platform for modeling SPG4 using CSMN-COs from isogenic hiPSCs. Unlike generic cortical organoids, our CSMN-COs uniquely replicate cellular populations specific to the motor

(E–F) Quantification of the SMI32-to-βIII-tubulin ratio in individual axons from 3-month (n = 8, (E)) and 6-month (n = 10, (F)) CSMN-COs. Tub A treatment significantly reduced SMI32 levels in mutant organoids.
(G–H) Quantification of HDAC6 enzymatic activity in 3-month (n = 3, (G)) and 6-month (n = 3, (H)) CSMN-COs from SPAST$^{WT/WT}$, SPAST$^{WT/S245X}$, and SPAST$^{WT/C448Y}$ lines, with or without Tub A treatment. HDAC6 activity is expressed as units (U) per mg of total protein, where one unit is defined as the amount of enzyme required to deacetylate 1 pmol of a synthetic acetylated peptide substrate per minute. Elevated HDAC6 activity in mutant organoids is significantly reduced by Tub A treatment at both time points.
(I–J) WB (I) and quantification (J) of HDAC6 (black arrow) protein levels in 3-month CSMN-COs derived from SPAST$^{WT/WT}$, SPAST$^{WT/S245X}$, and SPAST$^{WT/C448Y}$ lines. HDAC6 expression, normalized to GAPDH and shown relative to SPAST$^{WT/WT}$, revealed no significant differences across genotypes (n = 4).
One-way ANOVA with Tukey *post hoc* analysis. *p < 0.05, **p < 0.002, ***p < 0.001, ****p < 0.0001, and unpaired t test. ##p < 0.005, ###p < 0.001. All data shown as mean ± SD; see Tables S3 and S4 for details.

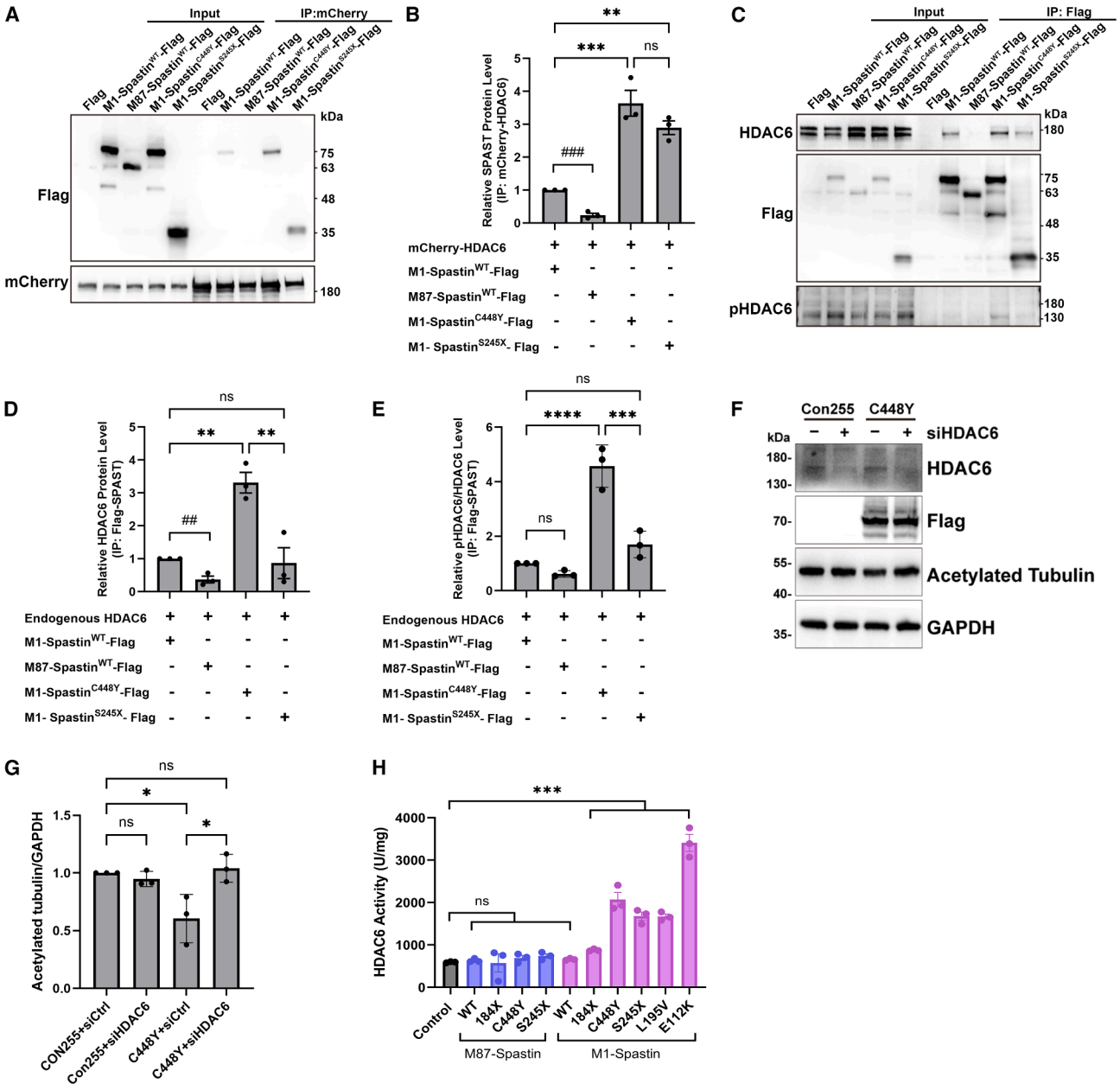

Figure 5. HDAC6 selectively interacts with M1-spastin and is aberrantly activated by mutant forms

(A and B) Co-immunoprecipitation (coIP) in HEK293T cells co-expressing HDAC6-mCherry and Flag-tagged spastin isoforms revealed that HDAC6 binds selectively to M1-spastin, but not M87-spastin (A). Quantification confirmed robust enrichment of M1-spastin isoforms in the HDAC6-containing immunoprecipitated complex, with significantly increased interaction observed for mutant forms (B).

(C–E) Reciprocal coIP using anti-Flag antibody was performed to isolate spastin isoforms, followed by WB with anti-HDAC6 and anti-phospho-HDAC6 antibodies, showing that M1-spastin^{C448Y}-Flag immunoprecipitated more phosphorylated HDAC6 (C). Quantification also confirmed that mutant M1-spastin isoforms pulled down greater amounts of HDAC6 compared to controls (D) and that M1-spastinC448Y-Flag immunoprecipitated more phosphorylated HDAC6 (E).

(F and G) Western blot analysis of 293T lysates showing levels of acetylated tubulin and GAPDH in Con255- and M1-C448Y-overexpressing cells treated with HDAC6 siRNA (siHDAC6) or control siRNA (siCtrl) (F). C448Y overexpression results in a notable decrease in acetylated tubulin, while siHDAC6 treatment significantly increases acetylated tubulin levels in C448Y-overexpressing cells (G). GAPDH levels remain unchanged across groups and serve as a loading control ($n = 3$ per group).

(H) HDAC6 activity assays in SH-SY5Y cells expressing various M1- and M87-spastin mutants showed that only M1 mutations led to significantly elevated HDAC6 enzymatic activity, indicating an isoform-specific gain-of-function effect ($n = 3$).

One-way ANOVA with Tukey *post hoc* analysis. $^{*}p < 0.05$, $^{**}p < 0.002$, $^{***}p < 0.001$, $^{****}p < 0.0001$. All data shown as mean ± SD; see Tables S5 and S6 for details.

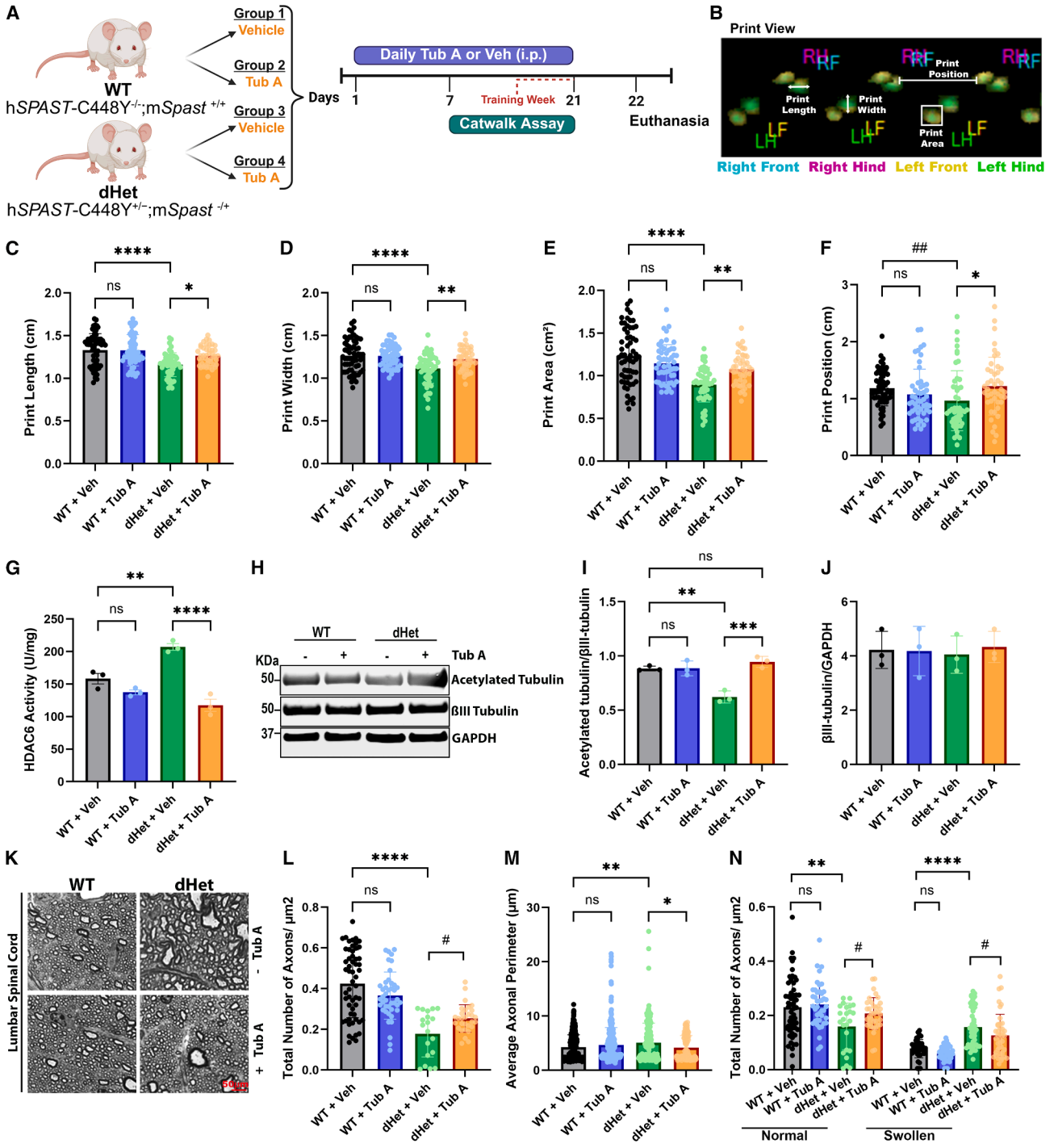

Figure 6. HDAC6 inhibition with Tub A improves gait deficiency and restores CST integrity in dHet mice

(A) Experimental timeline of daily Tub A or vehicle treatment and CatWalk analysis in WT and dHet mice.

(B) Representative CatWalk print view showing paw positioning and parameters analyzed, including print length, width, area, and position.

(C–F) Quantitative gait metrics across experimental groups: print length (C), print width (D), print area (E), and print position (F) (hind paw placement relative to the ipsilateral front paw). Data represent classified runs from 6 animals per group.

(G) HDAC6 enzymatic activity measured from spinal cord lysates across groups (n = 3 mice per group).

(H–J) WB analysis of lumbar spinal cord lysates showing levels of acetylated tubulin and βIII-tubulin in WT and dHet mice treated with Tub A or vehicle. Tub A treatment significantly increases acetylated tubulin levels in dHet mice. βIII-tubulin levels remain unchanged across groups and serve as a loading control (n = 3 per group).

(legend continued on next page)

cortex, particularly CSMNs, the primary neuronal subtype affected in SPG4.[37,64,65] Utilizing an isogenic background, this system enables precise interrogation of genotype-phenotype correlations for missense ($SPAST^{WT/C448Y}$) and truncation ($SPAST^{WT/S245X}$) mutations, addressing the previously elusive molecular underpinnings of clinical variability observed in SPG4.[50] Clinically, missense *SPAST* mutations generally cause earlier onset and more severe phenotypes compared to truncation mutations. Our findings align closely with these clinical discoveries, revealing accelerated and selective CSMN degeneration in $SPAST^{WT/C448Y}$ organoids. Although our CSMN-COs (1–6 months) model an early developmental stage, pathogenic *SPAST* mutations exert effects from the outset of neuronal differentiation. While clinical manifestations of SPG4 often appear in adulthood, this delay likely reflects compensatory mechanisms that operate *in vivo* across interconnected neuronal and non-neuronal systems. In contrast, our organoid model isolates cell-intrinsic processes, thereby revealing early molecular and structural abnormalities that may precede overt degeneration. The increased SMI32 immunoreactivity observed in mutant organoids reflects early axonal stress rather than neurite loss, consistent with a pre-degenerative state. Importantly, we did not observe axonal degeneration in 1-month-old organoids, indicating an age-dependent trajectory within this model. Moreover, several *de novo SPAST* mutations—particularly missense variants—are associated with childhood or infantile onset. Given that our mutations were introduced via CRISPR-Cas9, the observed early phenotypes may reflect such early-onset forms of the disease. Together, these considerations support the relevance of our organoid platform as a tractable model for early pathogenic mechanisms underlying SPG4.

Mechanistically, elevated *SPAST* mRNA levels were observed in both mutant organoids, confirming previous reports that *SPAST* mutations can escape nonsense-mediated decay.[51] The detection of the S245X truncated protein in our organoids, together with prior evidence that truncated M1-spastin is unusually stable,[22] suggests that truncation mutations may have effects beyond simple haploinsufficiency. Notably, both $SPAST^{WT/C448Y}$ and $SPAST^{WT/S245X}$ organoids show HDAC6 hyperactivation and microtubule hypoacetylation, features not observed in spastin-haploinsufficient models, further supporting the possibility of additional gain-of-function components. However, direct evidence remains limited, and additional studies will be needed to define the functional impact of these mutant isoforms. Furthermore, our coIP studies revealed that while both M1-$SPAST^{WT/S245X}$ and M1-$SPAST^{WT/C448Y}$ isoforms interact with HDAC6, the missense mutant M1-$SPAST^{WT/C448Y}$ exhibits markedly stronger binding, correlating with greater HDAC6 hyperactivation. This differential interaction suggests that distinct *SPAST* mutations may drive varying degrees of HDAC6 dysregulation which contributes to mutation-specific pathogenic severity in SPG4. Mutant M1-spastin may promote HDAC6 hyperactivation through two upstream mechanisms: by altering the stability or composition of the spastin-HDAC6 complex, which could enhance HDAC6 activity, or by inducing hyperactivation of casein kinase 2 (CK2), as previously identified in our studies,[27] which is suggested as an upstream enzyme that phosphorylates and further activates HDAC6.[66,67] Moreover, HDAC6 is not the only tubulin deacetylase; Sirtuin 2 and HDAC5 have also been shown to regulate microtubule acetylation[68,69] and exploring these upstream components may be valuable in uncovering the molecular underpinnings of SPG4 etiology. Furthermore, including more patient-derived hiPSC lines and additional *SPAST* mutations in our organoid models will be important for fully capturing SPG4's genetic and phenotypic diversity and advancing mechanistic and therapeutic insights. Our analysis using both CSMN-COs and transgenic mice revealed microtubule hypoacetylation as a key pathological feature in SPG4. This defect was significantly more pronounced in the missense mutant and closely correlated with greater neurodegenerative severity in patients with SPG4.[50,70] A prior study using a single, non-isogenic hiPSC line harboring an intronic splice-site *SPAST* mutation reported increased microtubule acetylation in 2D-cultured neurons, a result that differs from our findings.[71] Notably, this outcome phenocopies findings from spastin-depletion models, suggesting a phenotype driven predominantly by the haploinsufficiency mechanism in that context.[24,72,73] Indeed, both our isogenic organoid and transgenic mouse models consistently demonstrate HDAC6 hyperactivation, microtubule hypoacetylation, and axonal degeneration, supporting a shared pathogenic mechanism across SPG4 mutations. The use of complementary *in vitro* human and *in vivo* mouse systems is a key strength of this study, allowing validation of mechanistic findings across distinct yet biologically relevant contexts. Model-dependent features, such as aberrant neuronal activity in CSMN-COs and corticospinal tract or gait abnormalities in mice, reflect the distinct strengths and readouts of each system, thereby providing complementary and translational insights. Finally, our findings highlight HDAC6 hyperactivation, driven by mutant M1-spastin, as a convergent and therapeutically relevant mechanism in SPG4 pathogenesis. The ability of Tubastatin A to restore microtubule acetylation and ameliorate neurodegenerative phenotypes across both organoid and animal models underscores the translational potential of HDAC6 inhibition, offering a new avenue for therapeutic intervention for SPG4. The partial rescue achieved with HDAC6 inhibition in adult mice highlights promising avenues for future studies, including exploring combination therapies that could enhance therapeutic efficacy, especially in advanced stages of disease progression. Taken together, our study unveils corticospinal motor neuron enriched cortical organoids as a groundbreaking platform to decode the elusive corticospinal neuron vulnerability and advance targeted therapy development for SPG4 and other CSMN-related neurodegenerative diseases.

(K) Representative toluidine blue-stained cross-sections of the dorsal column in lumbar spinal cords from treated and untreated WT and dHet mice.
(L) Quantitative analyses of CST axons: total axon count per μm^2 (L), average axonal perimeter (M), and number of morphologically normal versus swollen axons (based on shape classification as normal: regular, swollen: irregular (N). Axons with a perimeter of $\geq$10 μm were considered swollen. Data represent cumulative axon counts (n = 120–500) from 3 mice per group.
One-way ANOVA with Tukey *post hoc* analysis. *$p < 0.05$, **$p < 0.002$, ***$p < 0.001$, ****$p < 0.0001$, and unpaired t test. #$p < 0.05$, ##$p < 0.005$. All data shown as mean ± SD; see Table S8 for details.

Limitations of the study

While our study provides significant insights into SPG4 pathology and therapeutic potential, several opportunities remain for future exploration. First, although our study modeled two *SPAST* variants (missense C448Y and truncation S245X) representing distinct mutation classes, inclusion of additional mutation types such as splice-site or frameshift variants will be necessary to fully capture the genetic and phenotypic diversity of SPG4. While our findings establish HDAC6 hyperactivation as a key mechanism in SPG4, the precise link between mutant M1-spastin and HDAC6 activation remains unclear. Additionally, HDAC6 acts on substrates beyond tubulin, which may also contribute to disease and merit further investigation. The partial rescue achieved with HDAC6 inhibition in adult mice highlights promising avenues for future studies, including exploring combination therapies that could enhance therapeutic efficacy, especially in advanced stages of disease progression. Lastly, while the present scRNA-seq analysis focused on validating cell-type composition and corticofugal neuron enrichment in control CSMN-COs, future work will extend this approach to mutant organoids. Comparative single-cell profiling will enable identification of cell type-specific transcriptional changes and pathway alterations underlying *SPAST*-related pathology. These forthcoming analyses will deepen mechanistic insight into early cellular vulnerability and network dysfunction in SPG4.

RESOURCE AVAILABILITY

Lead contact

Further information and requests for resources and reagents should be directed to and will be fulfilled by the lead contact, Liang Qiang (lq24@drexel.edu).

Materials availability

This study did not generate new unique reagents.

Data and code availability

- The scRNA-seq data used in this paper have been deposited in the National Center for Biotechnology Information Gene Expression Omnibus (NCBI-GEO) with the accession number GEO: GSE316534 and are publicly available as of the date of this publication.
- This paper does not report original code.
- Any additional information required to reanalyze the data reported in this paper is available from the lead contact upon request.

ACKNOWLEDGMENTS

We thank Angela Altadonna for assisting in breeding mice for the experiments and Larisa Ibric and Luisa Abadia for assisting with behavioral studies. We would like to thank the staff of the Columbia Stem Cell Initiative Stem Cell Core facility, under the leadership of Dr. Barbara Corneo at Columbia University Irving Medical Center for assisting with CRISPR-Cas9 editing for the work, including Dr. Grazia Iannello, Dr. Dario Sirabella, Dr. Achchhe Patel, Dr. Hemanta Sarmah, and Ms. Ekaterina Lebayle. We also want to thank Dr. Joanne Mathiasen for providing robust discussion and insights into dosing tubastatin A in mice, as well as Dr. Matthias Kneussel for providing the spastin knockout mice for breeding to generate the dHet mouse. All schematics were generated using BioRender. This research was supported by National Institutes of Health (R01NS115977), the 2020 SPF Foundation Grant, and a research grant funded by alsFINDaCURE and HOP on a CURE to L.Q.; by National Natural Science Foundation of China to M.L. (32070725); and by National Institutes of Health (R01NS118177) to P.W.B. Additional funding was provided by the Cure *SPG4* Foundation, the Lilly and Blair Foundation, *SPG4* Cure for Jack Laidlaw, and the Maurya Koduri Foundation.

AUTHOR CONTRIBUTIONS

L.Q., N.M., and M.L. conceived and designed the study. N.M. conducted all experiments, acquired and analyzed the data, and created the figures. S.R. performed injections, qPCR, and behavioral studies and analyzed scRNA-seq data. X.S. assisted in imaging and making figures for organoid studies. Y.S. conducted coIP studies. T.C. sectioned and stained spinal cords for mice anatomical studies. V.C. assisted in quantifications for organoid and behavioral studies. E.P. assisted in animal breeding and overexpression HDAC6 activity study. P.W.B. contributed to the conceptual discussion of the study, particularly transgenic mouse experiments, and provided tubastatin A as well as editorial input on the manuscript. J.C. provided insights and guidance in scRNA-seq experiments. L.Q. and N.M. wrote the manuscript. All authors reviewed and approved the manuscript for publication.

DECLARATION OF INTERESTS

The authors declare no other competing interests.

STAR★METHODS

Detailed methods are provided in the online version of this paper and include the following:

- KEY RESOURCES TABLE
- EXPERIMENTAL MODEL AND STUDY PARCITIPATION DETAILS
  - Isogenic SPG4-hiPSC generation, validation and maintenance
  - Corticospinal motor neurons enriched cortical organoid development and maintenance
  - SPG4-dHet transgenic mouse colony maintenance
- METHOD DETAILS
  - Organoid fixation, section and immunohistochemistry (IHC)
  - Single-cell RNA sequencing (scRNA-seq)
  - RNA Isolation and qRT-PCR
  - Multielectrode array (MEA) recording and analysis
  - Preparation and systemic delivery of tubastatin a in mice
  - Catwalk assay
  - Spinal cord tissue processing and quantitative axonal analysis
  - Whole blood collection and serum preparation
  - HDAC6 activity analysis
  - Spastin isoform overexpression in SH-SY5Y cells
  - Protein extraction and western blotting
  - Co-immunoprecipitation (Co-IP) and western blotting
  - HDAC6 knockdown
- QUANTIFICATION AND STATISTICAL ANALYSIS
  - Statistical analysis and data visualization

SUPPLEMENTAL INFORMATION

Supplemental information can be found online at https://doi.org/10.1016/j.celrep.2026.117036.

Received: July 31, 2025
Revised: December 3, 2025
Accepted: February 3, 2026

REFERENCES

1. Solowska, J.M., and Baas, P.W. (2015). Hereditary spastic paraplegia SPG4: what is known and not known about the disease. Brain *138*, 2471–2484. https://doi.org/10.1093/brain/awv178.

2. Shribman, S., Reid, E., Crosby, A.H., Houlden, H., and Warner, T.T. (2019). Hereditary spastic paraplegia: from diagnosis to emerging therapeutic approaches. Lancet Neurol. *18*, 1136–1146. https://doi.org/10.1016/s1474-4422(19)30235-2.

3. Blackstone, C. (2018). Converging cellular themes for the hereditary spastic paraplegias. Curr. Opin. Neurobiol. *51*, 139–146. https://doi.org/10.1016/j.conb.2018.04.025.

4. Reid, E. (2003). Science in motion: common molecular pathological themes emerge in the hereditary spastic paraplegias. J. Med. Genet. *40*, 81–86. https://doi.org/10.1136/jmg.40.2.81.

5. Ruano, L., Melo, C., Silva, M.C., and Coutinho, P. (2014). The global epidemiology of hereditary ataxia and spastic paraplegia: a systematic review of prevalence studies. Neuroepidemiology *42*, 174–183. https://doi.org/10.1159/000358801.

6. Mackay-Sim, A. (2021). Hereditary Spastic Paraplegia: From Genes, Cells and Networks to Novel Pathways for Drug Discovery. Brain Sci. *11*, 403. https://doi.org/10.3390/brainsci11030403.

7. Bruyn, R.P. (1992). The neuropathology of hereditary spastic paraparesis. Clin. Neurol. Neurosurg. *94*, S16–S18. https://doi.org/10.1016/0303-8467(92)90010-z.

8. Fink, J.K. (2014). Hereditary spastic paraplegia: clinical principles and genetic advances. Semin. Neurol. *34*, 293–305. https://doi.org/10.1055/s-0034-1386767.

9. Montanaro, D., Vavla, M., Frijia, F., Aghakhanyan, G., Baratto, A., Coi, A., Stefan, C., Girardi, G., Paparella, G., De Cori, S., et al. (2020). Multimodal MRI Longitudinal Assessment of White and Gray Matter in Different SPG Types of Hereditary Spastic Paraparesis. Front. Neurosci. *14*, 325. https://doi.org/10.3389/fnins.2020.00325.

10. White, K.D., Ince, P.G., Lusher, M., Lindsey, J., Cookson, M., Bashir, R., Shaw, P.J., and Bushby, K.M. (2000). Clinical and pathologic findings in hereditary spastic paraparesis with spastin mutation. Neurology *55*, 89–94. https://doi.org/10.1212/wnl.55.1.89.

11. Lo Giudice, T., Lombardi, F., Santorelli, F.M., Kawarai, T., and Orlacchio, A. (2014). Hereditary spastic paraplegia: clinical-genetic characteristics and evolving molecular mechanisms. Exp. Neurol. *261*, 518–539. https://doi.org/10.1016/j.expneurol.2014.06.011.

12. Salinas, S., Proukakis, C., Crosby, A., and Warner, T.T. (2008). Hereditary spastic paraplegia: clinical features and pathogenetic mechanisms. Lancet Neurol. *7*, 1127–1138. https://doi.org/10.1016/s1474-4422(08)70258-8.

13. Kuo, Y.W., Trottier, O., Mahamdeh, M., and Howard, J. (2019). Spastin is a dual-function enzyme that severs microtubules and promotes their regrowth to increase the number and mass of microtubules. Proc. Natl. Acad. Sci. USA *116*, 5533–5541. https://doi.org/10.1073/pnas.1818824116.

14. Yu, W., Qiang, L., Solowska, J.M., Karabay, A., Korulu, S., and Baas, P.W. (2008). The microtubule-severing proteins spastin and katanin participate differently in the formation of axonal branches. Mol. Biol. Cell *19*, 1485–1498. https://doi.org/10.1091/mbc.e07-09-0878.

15. Ji, Z., Zhang, G., Chen, L., Li, J., Yang, Y., Cha, C., Zhang, J., Lin, H., and Guo, G. (2018). Spastin Interacts with CRMP5 to Promote Neurite Outgrowth by Controlling the Microtubule Dynamics. Dev. Neurobiol. *78*, 1191–1205. https://doi.org/10.1002/dneu.22640.

16. Park, S.H., Zhu, P.P., Parker, R.L., and Blackstone, C. (2010). Hereditary spastic paraplegia proteins REEP1, spastin, and atlastin-1 coordinate microtubule interactions with the tubular ER network. J. Clin. Investig. *120*, 1097–1110. https://doi.org/10.1172/jci40979.

17. Wang, X., and O'Kane, C.J. (2008). Hereditary spastic paraplegia genes in Drosophila: dissecting their roles in axonal degeneration and intracellular traffic. SEB Exp. Biol. Ser. *60*, 161–182.

18. Papadopoulos, C., Orso, G., Mancuso, G., Herholz, M., Gumeni, S., Tadepalle, N., Jüngst, C., Tzschichholz, A., Schauss, A., Höning, S., et al. (2015). Spastin binds to lipid droplets and affects lipid metabolism. PLoS Genet. *11*, e1005149. https://doi.org/10.1371/journal.pgen.1005149.

19. Connell, J.W., Allison, R.J., Rodger, C.E., Pearson, G., Zlamalova, E., and Reid, E. (2020). ESCRT-III-associated proteins and spastin inhibit protrudin-dependent polarised membrane traffic. Cell. Mol. Life Sci. *77*, 2641–2658. https://doi.org/10.1007/s00018-019-03313-z.

20. Costa, A.C., and Sousa, M.M. (2022). The Role of Spastin in Axon Biology. Front. Cell Dev. Biol. *10*, 934522. https://doi.org/10.3389/fcell.2022.934522.

21. Solowska, J.M., D'Rozario, M., Jean, D.C., Davidson, M.W., Marenda, D.R., and Baas, P.W. (2014). Pathogenic mutation of spastin has gain-of-function effects on microtubule dynamics. J. Neurosci. *34*, 1856–1867. https://doi.org/10.1523/jneurosci.3309-13.2014.

22. Solowska, J.M., Rao, A.N., and Baas, P.W. (2017). Truncating mutations of SPAST associated with hereditary spastic paraplegia indicate greater accumulation and toxicity of the M1 isoform of spastin. Mol. Biol. Cell *28*, 1728–1737. https://doi.org/10.1091/mbc.E17-01-0047.

23. Qiang, L., Piermarini, E., Muralidharan, H., Yu, W., Leo, L., Hennessy, L.E., Fernandes, S., Connors, T., Yates, P.L., Swift, M., et al. (2019). Hereditary spastic paraplegia: gain-of-function mechanisms revealed by new transgenic mouse. Hum. Mol. Genet. *28*, 1136–1152. https://doi.org/10.1093/hmg/ddy419.

24. Piermarini, E., Akarsu, S., Connors, T., Kneussel, M., Lane, M.A., Morfini, G., Karabay, A., Baas, P.W., and Qiang, L. (2022). Modeling gain-of-function and loss-of-function components of SPAST-based hereditary spastic paraplegia using transgenic mice. Hum. Mol. Genet. *31*, 1844–1859. https://doi.org/10.1093/hmg/ddab367.

25. Ramakrishnan, S., Mohan, N., Dong, Z., Liu, M., and Qiang, L. (2025). Unraveling Isoform Complexity: The Roles of M1- and M87-Spastin in Spastic Paraplegia 4 (SPG4). Mov. Disord. *40*, 420–430. https://doi.org/10.1002/mds.30072.

26. Fonknechten, N., Mavel, D., Byrne, P., Davoine, C.S., Cruaud, C., Bönsch, D., Samson, D., Coutinho, P., Hutchinson, M., McMonagle, P., et al. (2000). Spectrum of SPG4 mutations in autosomal dominant spastic paraplegia. Hum. Mol. Genet. *9*, 637–644. https://doi.org/10.1093/hmg/9.4.637.

27. Leo, L., Weissmann, C., Burns, M., Kang, M., Song, Y., Qiang, L., Brady, S.T., Baas, P.W., and Morfini, G. (2017). Mutant spastin proteins promote deficits in axonal transport through an isoform-specific mechanism involving casein kinase 2 activation. Hum. Mol. Genet. *26*, 2321–2334. https://doi.org/10.1093/hmg/ddx125.

28. Osseni, A., Ravel-Chapuis, A., Thomas, J.L., Gache, V., Schaeffer, L., and Jasmin, B.J. (2020). HDAC6 regulates microtubule stability and clustering of AChRs at neuromuscular junctions. J. Cell Biol. *219*, e201901099. https://doi.org/10.1083/jcb.201901099.

29. Zhang, Y., Kwon, S., Yamaguchi, T., Cubizolles, F., Rousseaux, S., Kneissel, M., Cao, C., Li, N., Cheng, H.L., Chua, K., et al. (2008). Mice lacking histone deacetylase 6 have hyperacetylated tubulin but are viable and develop normally. Mol. Cell Biol. *28*, 1688–1701. https://doi.org/10.1128/mcb.01154-06.

30. Zhang, Y., Li, N., Caron, C., Matthias, G., Hess, D., Khochbin, S., and Matthias, P. (2003). HDAC-6 interacts with and deacetylates tubulin and microtubules in vivo. Embo j *22*, 1168–1179. https://doi.org/10.1093/emboj/cdg115.

31. Kalebic, N., Sorrentino, S., Perlas, E., Bolasco, G., Martinez, C., and Heppenstall, P.A. (2013). αTAT1 is the major α-tubulin acetyltransferase in mice. Nat. Commun. *4*, 1962. https://doi.org/10.1038/ncomms2962.

32. Trzeciakiewicz, H., Ajit, D., Tseng, J.H., Chen, Y., Ajit, A., Tabassum, Z., Lobrovich, R., Peterson, C., Riddick, N.V., Itano, M.S., et al. (2020). An HDAC6-dependent surveillance mechanism suppresses tau-mediated neurodegeneration and cognitive decline. Nat. Commun. *11*, 5522. https://doi.org/10.1038/s41467-020-19317-4.

33. Fazal, R., Boeynaems, S., Swijsen, A., De Decker, M., Fumagalli, L., Moisse, M., Vanneste, J., Guo, W., Boon, R., Vercruysse, T., et al. (2021). HDAC6 inhibition restores TDP-43 pathology and axonal transport defects in human motor neurons with TARDBP mutations. Embo j *40*, e106177. https://doi.org/10.15252/embj.2020106177.

34. Osseni, A., Ravel-Chapuis, A., Belotti, E., Scionti, I., Gangloff, Y.G., Moncollin, V., Mazelin, L., Mounier, R., Leblanc, P., Jasmin, B.J., and Schaeffer, L. (2022). Pharmacological inhibition of HDAC6 improves muscle phenotypes in dystrophin-deficient mice by downregulating TGF-β via Smad3 acetylation. Nat. Commun. *13*, 7108. https://doi.org/10.1038/s41467-022-34831-3.

35. d'Ydewalle, C., Krishnan, J., Chiheb, D.M., Van Damme, P., Irobi, J., Kozikowski, A.P., Vanden Berghe, P., Timmerman, V., Robberecht, W., and Van Den Bosch, L. (2011). HDAC6 inhibitors reverse axonal loss in a mouse model of mutant HSPB1-induced Charcot-Marie-Tooth disease. Nat. Med. *17*, 968–974. https://doi.org/10.1038/nm.2396.

36. Simões-Pires, C., Zwick, V., Nurisso, A., Schenker, E., Carrupt, P.A., and Cuendet, M. (2013). HDAC6 as a target for neurodegenerative diseases: what makes it different from the other HDACs? Mol. Neurodegener. *8*, 7. https://doi.org/10.1186/1750-1326-8-7.

37. McDermott, C.J., Burness, C.E., Kirby, J., Cox, L.E., Rao, D.G., Hewamadduma, C., Sharrack, B., Hadjivassiliou, M., Chinnery, P.F., Dalton, A., et al. (2006). Clinical features of hereditary spastic paraplegia due to spastin mutation. Neurology *67*, 45–51. https://doi.org/10.1212/01.wnl.0000223315.62404.00.

38. Lindsey, J.C., Lusher, M.E., McDermott, C.J., White, K.D., Reid, E., Rubinsztein, D.C., Bashir, R., Hazan, J., Shaw, P.J., and Bushby, K.M. (2000). Mutation analysis of the spastin gene (SPG4) in patients with hereditary spastic paraparesis. J. Med. Genet. *37*, 759–765. https://doi.org/10.1136/jmg.37.10.759.

39. Yates, P.L., Case, K., Sun, X., Sullivan, K., Baas, P.W., and Qiang, L. (2022). Veteran-derived cerebral organoids display multifaceted pathological defects in studies on Gulf War Illness. Front. Cell. Neurosci. *16*, 979652. https://doi.org/10.3389/fncel.2022.979652.

40. Sun, X., Kofman, S., Ogbolu, V.C., Karch, C.M., Ibric, L., and Qiang, L. (2024). Vascularized Brain Assembloids With Enhanced Cellular Complexity Provide Insights Into the Cellular Deficits of Tauopathy. Stem Cell. *42*, 107–115. https://doi.org/10.1093/stmcls/sxad086.

41. Cao, S.Y., Hu, Y., Chen, C., Yuan, F., Xu, M., Li, Q., Fang, K.H., Chen, Y., and Liu, Y. (2017). Enhanced derivation of human pluripotent stem cell-derived cortical glutamatergic neurons by a small molecule. Sci. Rep. *7*, 3282. https://doi.org/10.1038/s41598-017-03519-w.

42. Gaspard, N., Bouschet, T., Herpoel, A., Naeije, G., van den Ameele, J., and Vanderhaeghen, P. (2009). Generation of cortical neurons from mouse embryonic stem cells. Nat. Protoc. *4*, 1454–1463. https://doi.org/10.1038/nprot.2009.157.

43. Arlotta, P., Molyneaux, B.J., Chen, J., Inoue, J., Kominami, R., and Macklis, J.D. (2005). Neuronal subtype-specific genes that control corticospinal motor neuron development in vivo. Neuron *45*, 207–221. https://doi.org/10.1016/j.neuron.2004.12.036.

44. Pineda, S.S., Lee, H., Ulloa-Navas, M.J., Linville, R.M., Garcia, F.J., Galani, K., Engelberg-Cook, E., Castanedes, M.C., Fitzwalter, B.E., Pregent, L.J., et al. (2024). Single-cell dissection of the human motor and prefrontal cortices in ALS and FTLD. Cell *187*, 1971–1989.e16. https://doi.org/10.1016/j.cell.2024.02.031.

45. Samata, B., Takaichi, R., Ishii, Y., Fukushima, K., Nakagawa, H., Ono, Y., and Takahashi, J. (2020). L1CAM Is a Marker for Enriching Corticospinal Motor Neurons in the Developing Brain. Front. Cell. Neurosci. *14*, 31. https://doi.org/10.3389/fncel.2020.00031.

46. Genç, B., Jara, J.H., Sanchez, S.S., Lagrimas, A.K.B., Gözütok, Ö., Koçak, N., Zhu, Y., and Hande Özdinler, P. (2022). Upper motor neurons are a target for gene therapy and UCHL1 is necessary and sufficient to improve cellular integrity of diseased upper motor neurons. Gene Ther. *29*, 178–192. https://doi.org/10.1038/s41434-021-00303-4.

47. Yasvoina, M.V., Genç, B., Jara, J.H., Sheets, P.L., Quinlan, K.A., Milosevic, A., Shepherd, G.M.G., Heckman, C.J., and Özdinler, P.H. (2013). eGFP expression under UCHL1 promoter genetically labels corticospinal motor neurons and a subpopulation of degeneration-resistant spinal motor neurons in an ALS mouse model. J. Neurosci. *33*, 7890–7904. https://doi.org/10.1523/jneurosci.2787-12.2013.

48. Day, I.N.M., and Thompson, R.J. (2010). UCHL1 (PGP 9.5): neuronal biomarker and ubiquitin system protein. Prog. Neurobiol. *90*, 327–362. https://doi.org/10.1016/j.pneurobio.2009.10.020.

49. Osaka, H., Wang, Y.L., Takada, K., Takizawa, S., Setsuie, R., Li, H., Sato, Y., Nishikawa, K., Sun, Y.J., Sakurai, M., et al. (2003). Ubiquitin carboxy-terminal hydrolase L1 binds to and stabilizes monoubiquitin in neuron. Hum. Mol. Genet. *12*, 1945–1958. https://doi.org/10.1093/hmg/ddg211.

50. Parodi, L., Fenu, S., Barbier, M., Banneau, G., Duyckaerts, C., Tezenas du Montcel, S., Monin, M.L., Ait Said, S., Guegan, J., Tallaksen, C.M.E., et al. (2018). Spastic paraplegia due to SPAST mutations is modified by the underlying mutation and sex. Brain *141*, 3331–3342. https://doi.org/10.1093/brain/awy285.

51. Wang, J., Wu, Y., Dong, H., Ji, Y., Zhang, L., Liu, Y., Liu, Y., Gao, X., Jia, Y., and Wang, X. (2023). A novel truncated variant in SPAST results in spastin accumulation and defects in microtubule dynamics. BMC Med. Genomics *16*, 321. https://doi.org/10.1186/s12920-023-01759-6.

52. Errico, A., Ballabio, A., and Rugarli, E.I. (2002). Spastin, the protein mutated in autosomal dominant hereditary spastic paraplegia, is involved in microtubule dynamics. Hum. Mol. Genet. *11*, 153–163. https://doi.org/10.1093/hmg/11.2.153.

53. Yandamuri, S.S., and Lane, T.E. (2016). Imaging Axonal Degeneration and Repair in Preclinical Animal Models of Multiple Sclerosis. Front. Immunol. *7*, 189. https://doi.org/10.3389/fimmu.2016.00189.

54. Tsyba, D.L., Kirik, O.V., and Korzhevskii, D.E. (2021). SMI-32 — a novel axonal injury marker for investigation of ischemic brain pathology. MAJ *20*, 63–68. https://doi.org/10.17816/maj49849.

55. McIlwain, D.L., and Hoke, V.B. (2005). The role of the cytoskeleton in cell body enlargement, increased nuclear eccentricity and chromatolysis in axotomized spinal motor neurons. BMC Neurosci. *6*, 19. https://doi.org/10.1186/1471-2202-6-19.

56. Burgess, S.B., and McIlwain, D.L. (1994). Synchronous, intersegmental responses in motoneurons to lumbar ventral root injury. Neuroreport *5*, 2641–2644. https://doi.org/10.1097/00001756-199412000-00059.

57. Dehghani, A., Karatas, H., Can, A., Erdemli, E., Yemisci, M., Eren-Kocak, E., and Dalkara, T. (2018). Nuclear expansion and pore opening are instant signs of neuronal hypoxia and can identify poorly fixed brains. Sci. Rep. *8*, 14770. https://doi.org/10.1038/s41598-018-32878-1.

58. Heckenbach, I., Mkrtchyan, G.V., Ezra, M.B., Bakula, D., Madsen, J.S., Nielsen, M.H., Oró, D., Osborne, B., Covarrubias, A.J., Idda, M.L., et al. (2022). Nuclear morphology is a deep learning biomarker of cellular senescence. Nat. Aging *2*, 742–755. https://doi.org/10.1038/s43587-022-00263-3.

59. Leonhardt, M., Sellmer, A., Krämer, O.H., Dove, S., Elz, S., Kraus, B., Beyer, M., and Mahboobi, S. (2018). Design and biological evaluation of tetrahydro-β-carboline derivatives as highly potent histone deacetylase 6 (HDAC6) inhibitors. Eur. J. Med. Chem. *152*, 329–357. https://doi.org/10.1016/j.ejmech.2018.04.046.

60. Li, Z.Y., Zhang, C., Zhang, Y., Chen, L., Chen, B.D., Li, Q.Z., Zhang, X.J., and Li, W.P. (2017). A novel HDAC6 inhibitor Tubastatin A: Controls HDAC6-p97/VCP-mediated ubiquitination-autophagy turnover and reverses Temozolomide-induced ER stress-tolerance in GBM cells. Cancer Lett. *391*, 89–99. https://doi.org/10.1016/j.canlet.2017.01.025.

61. Shen, Z., Ji, K., Cai, Z., Huang, C., He, X., Xu, H., and Chen, G. (2021). Inhibition of HDAC6 by Tubastatin A reduces chondrocyte oxidative stress in chondrocytes and ameliorates mouse osteoarthritis by activating autophagy. Aging (Albany NY) *13*, 9820–9837. https://doi.org/10.18632/aging.202736.

62. Fang, M., Luo, L., Chen, Y., Liu, Y., Yan, Y., Wang, F., Zou, Y., Zhu, H., Wu, X., Jin, Z., et al. (2025). Perillaldehyde Improves Parkinson-Like Deficits by Targeting G3BP Mediated Stress Granule Assembly in Preclinical Models. Adv. Sci. *12*, e2412152. https://doi.org/10.1002/advs.202412152.

63. Wang, H.X., Deng, Z.A., Li, Y.Y., Li, J., Chen, Y.X., Zhao, Y.J., Huang, K.R., Tian, W.N., Tong, A.P., and Zhou, L.X. (2025). Inhibition of histone deacetylase 6 activity mitigates neurological impairment and post-hemorrhagic hydrocephalus after intraventricular hemorrhage by modulating pyroptosis and autophagy pathways. Fluids Barriers CNS *22*, 45. https://doi.org/10.1186/s12987-025-00658-5.

64. Rehbach, K., Kesavan, J., Hauser, S., Ritzenhofen, S., Jungverdorben, J., Schüle, R., Schöls, L., Peitz, M., and Brüstle, O. (2019). Multiparametric rapid screening of neuronal process pathology for drug target identification in HSP patient-specific neurons. Sci. Rep. *9*, 9615. https://doi.org/10.1038/s41598-019-45246-4.

65. Navas-Sánchez, F.J., Martín De Blas, D., Fernández-Pena, A., Alemán-Gómez, Y., Lage-Castellanos, A., Marcos-Vidal, L., Guzmán-De-Villoria, J.A., Catalina, I., Lillo, L., Muñoz-Blanco, J.L., et al. (2022). Corticospinal tract and motor cortex degeneration in pure hereditary spastic paraparesis type 4 (SPG4). Amyotroph. Lateral Scler. Frontotemporal Degener. *23*, 25–34. https://doi.org/10.1080/21678421.2021.1962353.

66. Li, Y., Shin, D., and Kwon, S.H. (2013). Histone deacetylase 6 plays a role as a distinct regulator of diverse cellular processes. FEBS J. *280*, 775–793. https://doi.org/10.1111/febs.12079.

67. Watabe, M., and Nakaki, T. (2011). Protein kinase CK2 regulates the formation and clearance of aggresomes in response to stress. J. Cell Sci. *124*, 1519–1532. https://doi.org/10.1242/jcs.081778.

68. Nagai, T., Ikeda, M., Chiba, S., Kanno, S.I., and Mizuno, K. (2013). Furry promotes acetylation of microtubules in the mitotic spindle by inhibition of SIRT2 tubulin deacetylase. J. Cell Sci. *126*, 4369–4380. https://doi.org/10.1242/jcs.127209.

69. Cho, Y., and Cavalli, V. (2012). HDAC5 is a novel injury-regulated tubulin deacetylase controlling axon regeneration. Embo j *31*, 3063–3078. https://doi.org/10.1038/emboj.2012.160.

70. Plaud, C., Joshi, V., Kajevu, N., Poüs, C., Curmi, P.A., and Burgo, A. (2018). Functional differences of short and long isoforms of spastin harboring missense mutation. Dis. Model. Mech. *11*, dmm033704. https://doi.org/10.1242/dmm.033704.

71. Denton, K.R., Lei, L., Grenier, J., Rodionov, V., Blackstone, C., and Li, X.J. (2014). Loss of spastin function results in disease-specific axonal defects in human pluripotent stem cell-based models of hereditary spastic paraplegia. Stem Cell. *32*, 414–423. https://doi.org/10.1002/stem.1569.

72. Trotta, N., Orso, G., Rossetto, M.G., Daga, A., and Broadie, K. (2004). The hereditary spastic paraplegia gene, spastin, regulates microtubule stability to modulate synaptic structure and function. Curr. Biol. *14*, 1135–1147. https://doi.org/10.1016/j.cub.2004.06.058.

73. Fassier, C., Tarrade, A., Peris, L., Courageot, S., Mailly, P., Dalard, C., Delga, S., Roblot, N., Lefèvre, J., Job, D., et al. (2013). Microtubule-targeting drugs rescue axonal swellings in cortical neurons from spastin knockout mice. Dis. Model. Mech. *6*, 72–83. https://doi.org/10.1242/dmm.008946.

74. Patel, A., Garcia Diaz, A., Moore, J.C., Sirabella, D., and Corneo, B. (2020). Establishment and characterization of two iPSC lines derived from healthy controls. Stem Cell Res. *47*, 101926. https://doi.org/10.1016/j.scr.2020.101926.

75. Yates, P.L., Patil, A., Sun, X., Niceforo, A., Gill, R., Callahan, P., Beck, W., Piermarini, E., Terry, A.V., Sullivan, K.A., et al. (2021). A cellular approach to understanding and treating Gulf War Illness. Cell. Mol. Life Sci. *78*, 6941–6961. https://doi.org/10.1007/s00018-021-03942-3.

76. Serrao, M., Rinaldi, M., Ranavolo, A., Lacquaniti, F., Martino, G., Leonardi, L., Conte, C., Varrecchia, T., Draicchio, F., Coppola, G., et al. (2016). Gait Patterns in Patients with Hereditary Spastic Paraparesis. PLoS One *11*, e0164623. https://doi.org/10.1371/journal.pone.0164623.

77. Parasuraman, S., Raveendran, R., and Kesavan, R. (2010). Blood sample collection in small laboratory animals. J. Pharmacol. Pharmacother. *1*, 87–93. https://doi.org/10.4103/0976-500x.72350.

STAR★METHODS

KEY RESOURCES TABLE

REAGENT or RESOURCE	SOURCE	IDENTIFIER
Antibodies		
SOX2	R&D Systems	Cat# AF2018; RRID:AB_355110
Neun	Abcam	Cat# ab104224; RRID:AB_10711040
MAP2	Novus Biologicals	NB300-213 Cat# NB300-213; RRID:AB_2138178
βIII- Tubulin	BioLegend	Cat# 802001; RRID:AB_2564645
CTIP2	Abcam	Cat# ab18465; RRID:AB_2064130
GFAP	Abcam	Cat# ab53554; RRID:AB_880202
SMI312	BioLegend	Cat# 837904; RRID:AB_2566782
L1CAM	BioLegend	Cat# 371607; RRID:AB_2734424
vGlut1	Synaptic Systems	Cat# 135 302; RRID:AB_887877
Synaptophysin	Proteintech	Proteintech Cat# 60191-1-Ig; RRID:AB_10915965
SMI32	BioLegend	Cat# 801701; RRID:AB_2564642
Acetylated Tubulin	Sigma-Aldrich	Cat# T6793; RRID:AB_477585
HDAC6	Cell Signaling Technology	Cat# 7612; RRID:AB_10889735
βIII- Tubulin	Abcam	Cat# ab7751; RRID:AB_306045
GAPDH	Abcam	Cat# ab8245; RRID:AB_2107448
Spastin	Abcam	Cat# ab77144; RRID:AB_1524436
Anti-Flag	Proteintech	Cat# 20543-1-AP; RRID:AB_11232216
Anti-Phosphoserine/threonine	PhosphoSolutions	Cat# PP2551; RRID:AB_1184778
Anti-HDAC6	Affinity Biosciences	Cat# AF6485; RRID:AB_2835165
Anti-mCherry	Abcam	Cat# ab205402; RRID:AB_2722769
Chemicals, peptides, and recombinant proteins		
MTeSR™ Plus	Stem Cell Technologies	100–0276
DMEM-F12	Gibco	11330032
ReLeSR™	Stem Cell Technologies	100–0483
ROCK inhibitor Y-27632	Tocris	1254
Dorsomorphin	Sigma	C956T21
SB431542	Tocris	1614
Neurobasal A	Thermo Fisher	10-888- 022
B-27 without Vitamin A	Thermo Fisher	12587010
Glutamax	Thermo Fisher	35- 050-061
EGF	PeproTech	AF-100-15
bFGF	Peprotech	100-18B
Cyclopamine	Fisher Scientific	AAJ61528MB
B-27 Plus	Thermo Fisher Scientific	A3582801
Normocin	InvivoGen	ant-nr-05
BDNF	PeproTech	450–02
NT3	PeproTech	450–03
StemPro Accutase™ Cell Dissociation Reagent	Thermo Fisher Scientific	A1110501
DNAase I	Thermo Fisher Scientific	EN0521
BrainPhys Neuronal Medium	Stem Cell Technologies	05790
Tubastatin A	Selleckchem	S8049
Paraformaldehyde	Electron Microscopy Sciences	19202
Fetal bovine serum	Novus Biologicals	S11150

(*Continued on next page*)

Continued

REAGENT or RESOURCE	SOURCE	IDENTIFIER
Lipofectamine 2000	Invitrogen	11668–019
1X RIPA Buffer	Thermo Fisher Scientific	89900
Halt™ Protease and Phosphatase Inhibitor Cocktail	Thermo Fisher Scientific	78446
IP cell lysis buffer	Thermo Fisher	87787
Protease inhibitor	NCM Biotech	P001
Phosphatase inhibitor	NCM Biotech	P003
Critical commercial assays		
HDAC6 Fluorogenic Assay	BPS Biosciences	50076–1
PureLink™ RNA Mini Kit	Thermo Fisher Scientific	12183018A
High-Capacity cDNA Reverse Transcription Kit	Thermo Fisher Scientific	4368813
BCA Protein Assay Kit	Thermo Fisher Scientific	23227
Deposited Data		
scRNAseq data	NCBI GEO	GEO: GSE316534
Experimental models: Cell lines		
Isogenic Spastin hiPSCs	Generated in Lab from a control hiPSC. This paper	N/A
SH-SY5Y neuroblastoma cell line	ATCC	CRL-2266
293T cells	Chinese Academy of Science (National Collection of Authenticated Cell Cultures)	GNHu17
Experimental models: Organisms/strains		
Mouse: hSPAST-C448Y$^{+/-}$; mSPAST$^{\Delta/+}$).	Piermarini et al.,[24] Generated in Lab	N/A
Oligonucleotides		
CTIP2FWD: ATGTCCCGCCGCAAACA REV: TCGTCTTCTTCGAGGATGG	Integrated DNA Technologies, Inc.	N/A
L1CAMFWD: GTCCACTACACCTTTAGGGTTAC REV: CTTCACATCCACAGGGTTCTT	Integrated DNA Technologies, Inc.	N/A
CRYMFWD: GAGCTGGGAGAAGTGATTAAGG REV: TGGCTGCAACTGTGTCTT	Integrated DNA Technologies, Inc.	N/A
vGlut1FWD: CACTCAGATTCCAGGAGGATTT REV: CGAAGATGACACAGCCATAGT	Integrated DNA Technologies, Inc.	N/A
UCLH1FWD: CCAATGTCGGGTAGATGACAAG REV: AGGCATTCGTCCATCAAGTTC	Integrated DNA Technologies, Inc.	N/A
N-terminal SpastinFWD: CAGAAGGAGCAAGCTGT GGAREV: GTAAGCGGTCCTTGGCCATA	Integrated DNA Technologies, Inc.	N/A
C-terminal Spastin FWD: AGAAGAGAAGGGGA GCACGA REV: AAACGCCTGAGAACAGCCTC	Integrated DNA Technologies, Inc.	N/A
GAPDHFWD: TCGGAGTCAACGGATTTGGT REV: TTCCCGTTCTCAGCCTTGAC	Integrated DNA Technologies, Inc.	N/A
HDAC6 siRNAGUGUUGGAUGAGCAGUUAAAUTT AUUUAACUGCUCAUCCAACACTT	Integrated DNA Technologies, Inc.	N/A
Recombinant DNA		
Wildtype M87	Solowska et al.[22]	Addgene, 89322
M87 184X	Solowska et al.[22]	Addgene, 92367
M87 C448Y	Solowska et al.[22]	Addgene, 89320
M87 S245X	Solowska et al.[22]	Addgene, 92368
Wildtype M1	Solowska et al.[22]	Addgene, 89321
M1 184X	Solowska et al.[22]	Addgene, 92365
M1 C448Y	Solowska et al.[22]	Addgene, 89319
M1 S245X	Solowska et al.[22]	Addgene, 92366
M1 L195V-Myc tagged	Solowska et al.[22]	Addgene, 87716

(*Continued on next page*)

Continued		
REAGENT or RESOURCE	SOURCE	IDENTIFIER
M1 E112K-Myc tagged	Solowska et al.[22]	Addgene, 87715
mcherry-HDAC6	This paper	N/A
CON255-Flag	This paper	N/A
M1-Spastin^{WT}-Flag	This paper	N/A
M87-Spastin^{WT}-Flag	This paper	N/A
M1-Spastin^{C448Y}-Flag	This paper	N/A
M1-Spastin^{S245X}-Flag	This paper	N/A
Software and algorithms		
ImageJ	NIH	https://imagej.nih.gov/ij/
Cell Ranger Count v7.0.1	10X Genomics, Cloud analysis	N/A
Partek Flow software with scRNAseq toolkit	Illumina	N/A
GraphPad Prism version 10	N/A	N/A
Adobe Photoshop 2024	Adobe Creative Cloud	
EndNote 21	N/A	N/A
BioRender	N/A	N/A

EXPERIMENTAL MODEL AND STUDY PARCITIPATION DETAILS

Isogenic SPG4-hiPSC generation, validation and maintenance

Isogenic human induced pluripotent stem cells (hiPSCs) were derived from a control hiPSC line (FA0000010) which was generated from a healthy 36-year-old male donor using previously established protocols obtained from the Columbia Stem Cell Initiative Stem Cell Core facility.[74] CRISPR (Clustered regularly interspaced short palindromic repeat) – Cas9 (CRISPR-associated protein 9) genome editing was employed to generate isogenic hiPSC lines harboring two distinct disease-associated mutations in the SPAST gene. Highly specific single-guide RNAs (sgRNAs) were designed to target defined loci within SPAST, enabling precise introduction of pathogenic variants via homology-directed repair, while preserving genomic integrity at off-target sites. All hiPSC lines and subcolonies were authenticated as described below and tested negative for mycoplasma contamination. The lines were validated for their pluripotency by immunostaining for OCT4, SSEA-4, SOX2, and TRA1-60 (Thermo Fisher Scientific, A24881). Germ layer differentiation was conducted using the Human Pluripotent Stem Cell Functional Identification Kit (R&D Systems, SC027B) and G-banded karyotype and mutation analysis was also carried out to confirm CRISPR-Cas9 based mutation. All hiPSC lines were cultured in 5% CO_2 at 37°C in mTeSR Plus (Stem Cell Technologies, 100–0276) on Matrigel GFR Basement Membrane Matrix (Corning, 356231) as previously reported.[40] Briefly, 6- well plate (Thermo Scientific, 140675) was coated with Matrigel diluted in ice-cold DMEM-F12 (Gibco, 11330032) for 1 h at 37°C. Once all hiPSCs reach 70% confluence, they are passaged using ReLeSR (Stem Cell Technologies, 100–0483), incubated for 4 min and subsequently plated on coated dishes with 10μM ROCK inhibitor Y-27632 (Tocris, 1254). 3mL Medium changes with mTeSR Plus was performed every other day.

Corticospinal motor neurons enriched cortical organoid development and maintenance

Organoids were generated using a modified version of the previously reported publication.[39,40] Briefly, on day 0, pure and 90% confluent hiPSCs were lifted using ReLeSR for 4 min and plated onto ultra-low attachment 6- well plate (Corning, 3471) in mTeSR Plus with 10μM ROCK inhibitor Y-27632, 5μM Dorsomorphin (Sigma, C956T21), and 10μM SB431542 (Tocris, 1614) to promote embryoid bodies (EBs) formation. From day 3–6, a half medium changes with Dorsomorphin and SB431542 in mTeSR Plus was performed every other day. From days 7–23, half medium change was performed using neuronal differentiation media I which consist of Neurobasal A (Thermo Fisher, 10-888- 022), B-27 without Vitamin A (Thermo Fisher, 12587010), Glutamax (Thermo Fisher, 35- 050–061), 20ng/mL EGF (PeproTech, AF-100-15), 20ng/mL bFGF (Peprotech, 100-18B), particularly with 5μM cyclopamine (Fisher Scientific, AAJ61528MB). On day 23, organoids were placed on an orbital shaker (60 rpm) and the medium was switched to neuronal differentiation media II which consists of Neurobasal A (Thermo Fisher, 10-888- 022), B-27 Plus (Thermo Fisher Scientific, A3582801), Glutamax (Thermo Fisher, 35- 050–061), Normocin (InvivoGen, ant-nr-05), 20 ng/mL BDNF (PeproTech, 450-02) and 20 ng/mL NT3 (PeproTech, 450-03). All organoids were cultured in 5% CO2 at 37°C on an orbital shaker. Medium changes were performed every 3–4 days.

SPG4-dHet transgenic mouse colony maintenance

All the transgenic mouse experiments were performed in compliance with the NIH's Guide for the Care and Use of Laboratory Animals and were reviewed and approved by the Institutional Animal Care and Use Committee at Drexel University. Five mice were housed per cage under a 12-h light/dark cycle, temperature and humidity were kept constant, and mice had free access to drinking water and food. Colony generation, breeding strategies, and genotyping are all previously described in detail.[23,24] For this study, we used our novel male double-heterozygous mice (dHet) that contains one copy of human mutant SPAST^{C448Y} at Rosa26 locus and one copy of endogenous mouse *Spast* (hSPAST-C448Y$^{+/-}$; mSpast$^{-/+}$) which depicts both CST dieback and adult-onset gait deficiencies that are remarkably reminiscent of human patients.[24]

METHOD DETAILS

Organoid fixation, section and immunohistochemistry (IHC)

Organoids were washed once with PBS (Gibco, 10010023) and fixed in 4% PFA overnight at 4°C followed by dehydration in 30% sucrose until fully saturated. Organoids were then embedded in M1 Embedding Matrix (Epredia, 1310) and cryosectioned at 25μm thickness and placed on charged slides (Fisher Scientific, 1255016). The slides were dried at room temperature overnight. Organoid mounted slides were then hydrated and washed in 1X PBS 3 times for 5 min followed by quenching (70% PBS, 30% methanol, 0.5% hydrogen peroxide) for 1 h at room temperature. Subsequently, the slides were washed in PBS to remove the quenching buffer and incubated in either donkey (Jackson ImmunoResearch, 017-000-121) or goat (Jackson ImmunoResearch, 005-000-121) serum blocking buffer diluted in PBS for 1 h at room temperature. Then primary antibodies listed in key resource table diluted in PBS and 0.1% Triton X-100 was incubated overnight at 4°C followed by PBS washes and corresponding secondary antibodies conjugated to Alexa Fluor 488, 555, or 647 incubated for 2 h at room temperature. Lastly, the slides were washed in PBS and incubated with DAPI at 1:20,000 dilution (Fisher Scientific, D1306) and mounted using Fluoro-Gel with Tris Buffer (Electron Microscopy Sciences 1798510). Organoid sections were imaged using Leica SP8 inverted confocal microscope and Leica Thunder microscope. ImageJ was used to measure average fluorescence intensity of each organoid section and individual neuronal processes.

Single-cell RNA sequencing (scRNA-seq)

10X Chromium Next GEM single cell 3′ Gene expression kit V3.1 dual index kit and 10X Chromium Controller system was used to generate single cell data. Briefly, 3-month-old organoids were dissociated using 4 mL StemPro Accutase Cell Dissociation Reagent (Thermo Fisher Scientific, A1110501) for 12 min at 37°C. Subsequently, the organoids were quenched and treated briefly with DNAase I (Thermo Fisher Scientific, EN0521) and gently triturated using 2mL serological pipettes to generate single cell suspension in PBS with 1% BSA. Cell viability and count were assessed using trypan blue staining and a hemocytometer. The cell suspension was then loaded onto Chromium next GEM Chip G (10x Genomics, 2000177) per manufacturer instructions, with a targeted cell recovery of 5000–10000 cells. Post GEM formation, the samples were subjected to reverse transcription, amplification, fragmentation and clean-ups, as recommended by the manufacturer. We then performed Illumina library preparation using the Dual Index plate TT Set A (10X Genomics, 3000431; Plate, 15535894). The subsequent library was then sequenced using NovaSeq6000 at a depth of 25000–30000 paired end reads per cell.

Raw sequencing data were initially processed and aligned to GRCh38 (human) using Cell Ranger Count v7.0.1 (10X Genomics, Cloud analysis) and HDF5 files were generated. The HDF5 files were then uploaded to the Partek Flow software with scRNAseq toolkit (Illumina). Using a single cell QA/QC and a noise-reduction pipeline, the cells were further filtered to exclude low quality cells and features. The filtered set was then normalized using the recommended counts per million, add 1, log 2 transformation workflow. Principal component analysis (PCA) was performed on the filtered cells and further clustered using Louvain graph-based clustering algorithm using the top 20 PCAs and visualized using uniform manifold approximation and projection (UMAP). We then extracted the biomarkers for these clusters and used them to manually annotate the clusters. Panglao database, Human protein atlas and extensive literature review were used to annotate the seven clusters as neuroepithelial cells, glial cells, intermediate progenitor cells, corticospinal motor neurons, deep layer excitatory neurons, GABAergic neurons and glutamatergic neurons. A heatmap was generated using the marker genes of each cell cluster. Gene expression profile of various marker genes was generated using the same 2D UMAP as cluster annotations.

RNA Isolation and qRT-PCR

RNA was isolated from various organoid samples using the PureLink RNA Mini Kit (Thermo Fisher Scientific, 12183018A) and subsequently reverse transcription was performed using the High-Capacity cDNA Reverse Transcription Kit (Thermo Fisher Scientific, 4368813) to synthesize cDNA. Quality control and quantification was performed using the NanoDrop Spectrophotometer. qRT-PCR was performed using the 2X Universal SYBR Green Fast qPCR Mix (ABclonal, RK21203) on the StepOnePlus Real-Time PCR System (Applied Biosystems). RNA primers were acquired from Integrated DNA Technologies and listed in key resource table.

Multielectrode array (MEA) recording and analysis

Single-wells containing 60 electrodes (Multi Channel Systems, MEA2100-Systems), were coated with Poly-L-Ornithine (Sigma Aldrich, P4957) overnight at room temperature then washed 3–5 times with sterile ddH_2O. The wells were fully dried, and organoids

were placed centrally covering all the electrodes and cultured in BrainPhys Neuronal Medium (Stem Cell Technologies, 05790) supplemented with BDNF and NT3. Two days after organoid placement, extracellular spontaneous neuronal activity was recorded for a duration of 5 min using the Multi-Channel Experimenter software as previously described.[75] The recording parameter was acquired at 20 kHz and filtered with a 3500 Hz fourth-order high-pass Butterworth filter and neuronal spikes were detected when the signals surpassed a threshold of 6 standard deviations from the baseline noise. Bursts were detected when $\geq$4 spikes with a duration of 50 milliseconds (ms) and an interval of 100ms between bursts occurred. Network bursts were detected when a minimum of 10 electrodes were active with 5 of them simultaneously participating. Acquired data was processed using Multi Channel Analyzer and organized in Microsoft Excel.

Preparation and systemic delivery of tubastatin a in mice

Tubastatin A (Selleckchem, S8049, Batch: S804913) was prepared according to manufacturer's instructions. Animals were administrated Tub A in 5% DMSO and 95% corn oil at a dose of 16mg/kg with a dosing volume of 10mL/kg daily for 21 days intraperitoneally. A mixture of DMSO and corn oil was used as a vehicle. After 21 days of treatment, animals were euthanized for biochemical analysis. For organoid studies, 100μM Tub A in DMSO was added to the culture media daily for 72 h and collected for downstream analysis.

Catwalk assay

The Noldus Catwalk XT is an automated gait analysis system for assessing locomotion in rats and mice. The behavioral platform and procedure were previously described in great detail.[23,24] Briefly, mice were isolated in the behavior room 30 min prior to testing to acclimate them to the new environment. Each mouse underwent a week of training where they learned the task following a week of recording for the various gait parameter analysis. Animals were individually placed on the catwalk to freely move in both directions. After 15 min, the animal was removed from the walkway and returned to its home cage. The camera gain was set to 20dB and the detection threshold was set to 0.10. Compliant runs were classified as run with a duration between 0.50 and 5.00 s with a maximum speed variation of 60%. For each animal, 5–6 compliant runs per group were used for analysis. For consistency and rigor, both training and recording were conducted by the same person. Five to 6 animals per group were used for behavioral studies. Clinically relevant parameters were chosen for analysis for this study.[24,76]

Spinal cord tissue processing and quantitative axonal analysis

Spinal cord tissue collection, processing, and anatomical analysis were performed as previously described.[23,24] For anatomical analysis in this study, three mice per group were sacrificed by intraperitoneal injection of 150 mg/kg Euthasol solution (VEDCO, 50989056912). Transcardial perfusion was performed using a buffered 0.9% NaCl rinse followed by tissue fixation in a mixture of 4% paraformaldehyde (PFA; Electron Microscopy Sciences, 19202) and 1% Glutaraldehyde in 0.1M phosphate buffer. Spinal cords were dissected out and were post-fixed overnight at 4°C in the same fixative solution. Cords were then washed in 0.1M phosphate buffer overnight at 4°C and cervical and lumbar blocks of spinal cord were sectioned at 200μm using a Vibratome. Sectioned cords were further post-fixed in cold buffered 2% osmium tetroxide for 1 h followed by sequential dehydration in 70, 95 and 100% ethanol followed by two rinses in propylene oxide (PO). The cords were then incubated in a 1:1 mixture of Epon -Araldite and PO for 1 h followed by a 2:1 mixture of Epon-Araldite and PO overnight and lastly incubated in 100% Epon-Araldite with 2% DMP-30 hardener for 2 h. The spinal cord sections were finally embedded in fresh Epon-Araldite with 2% DMP-30 hardener in silicone molds and allowed to polymerize for 72 h in a 60°C oven. 1μm sections were cut from each block using a glass knife mounted on an ultramicrotome and sections were stained with toluidine blue to visualize cross-sections of axons. The corticospinal tract located in the most ventral part of the dorsal column was imaged using Axio Observer 7 Zeiss microscope with a 100X objective. Axonal count and perimeter were quantified using ImageJ.

Whole blood collection and serum preparation

Whole blood was collected from 3 mice per group. Whole blood was collected through a transcardial puncture and processed in Vacutainer Serum Tubes (Becton Dickinson, 366668) following a previously published protocol.[77] To isolate the serum from whole blood, the blood was incubated at room temperature for 15 min to clot and centrifuged for 10 min at 4°C at 3000g. The resulting supernatant was collected and sent to the Animal Diagnostic Laboratory at the University of Michigan Medical School- Pathology Core for biochemical analysis to assess hepatotoxicity.

HDAC6 activity analysis

HDAC6 activity assays were performed according to the manufacturer's instructions (BPS Biosciences, 50076-1) and as previously described.[23,24] Briefly, treated and untreated organoid samples, as well as spinal cord tissue samples, were lysed in HDCA6 lysis buffer and centrifuged at 16,000g for 10 min at 4°C. The protein content resulting from the supernatant was quantified using the Pierce BCA Protein Assay Kit (Thermo Fisher Scientific, 23227). Samples were then incubated at 37°C for 30 min with HDAC6 substrate followed by incubating the developer for 10 min at 37°C to stop the reaction. The fluorescence was measured on a Tecan spectral plate reader at 380/490nm (excitation/emission). The analysis was conducted per the manufacturer's instructions where the

results are expressed as U per mg of protein, where U stands for the amount of HDAC6 required to deacetylate 1pmol of HDAC6 substrate per min.

Spastin isoform overexpression in SH-SY5Y cells

SH-SY5Y neuroblastoma cell line was used to overexpress either wild-type or mutant forms of M1-spastin or M87-spastin as listed in key resource table. Cells were cultured in DMEM/F12 medium (Thermo Fisher Scientific, 11320033) supplemented with 10% fetal bovine serum (Novus Biologicals, S11150) and 1% penicillin-streptomycin (Pen/Strep, 100 IU/mL and 100 μg/mL), and plated in 100mm culture dishes (BD Falcon, 353003). At 60–70% confluency, cells were transfected with 2μg of wildtype or mutant M1/M87 constructs using Lipofectamine 2000 (Invitrogen, 11668-019) according to the manufacturer's instructions. 72 h post transfection, cells were harvested in ice-cold PBS and centrifuged at 1500 rpm × 5 min at room temperature. The resulting cell pellets were further lysed and used for HDAC6 activity assays (see above). Non-transfected (naive) SH-SY5Y cells were included as control.

Protein extraction and western blotting

Organoid samples were lysed in 1X RIPA Buffer (Thermo Fisher Scientific, 89900) supplemented with Halt Protease and Phosphatase Inhibitor Cocktail (Thermo Fisher Scientific, 78446). For animal studies, the mice are euthanized as described above and the motor cortex and spinal cords were dissected and homogenized in the same RIPA buffer with inhibitors. All samples were sonicated on ice with two 30-s on/off pulses, then centrifuged at 15,000 × g for 30 min at 4°C. The supernatant was collected and total protein concentration determined using the Pierce BCA Protein Assay Kit (Thermo Fisher Scientific, 23227). Equal amounts of protein (25 μg per sample) from both organoid and mouse tissue lysates were combined with 4X LDS sample buffer (Thermo Fisher Scientific, B0007) and 10X Sample Reducing Agent (Thermo Fisher Scientific, B0009), and then subjected to SDS-PAGE on 4–12% Bis-Tris Plus gels (Thermo Fisher Scientific, NW04120BOX). Proteins were transferred onto PVDF membranes (Thermo Fisher Scientific, 88518) using either a 0.34 A constant current for 2 h (instant transfer) or 0.1 A overnight on ice. Following transfer, membranes were blocked at room temperature for 1 h in LI-COR blocking buffer (Li-co Bioscience, 927–60010), then incubated overnight at 4°C with primary antibodies as listed in key resource table. The next day, membranes were incubated with fluorescent secondary antibodies (LI-COR IRDye 680RD or IRDye 800CW)) for 2 h at room temperature on a shaker. Protein bands were visualized using the Odyssey DLx Infrared Imaging System (LI-COR), and band intensities quantified using Fiji (ImageJ).

Co-immunoprecipitation (Co-IP) and western blotting

Co-immunoprecipitation was performed to investigate potential interactions between HDAC6 and spastin isoforms. Due to the lack of suitable antibodies for immunoprecipitating endogenous spastin and HDAC6, epitope-tagged expression constructs were employed. HEK293T cells were co-transfected with mcherry-HDAC6 and one of the following Tet-on, FLAG-tagged spastin constructs: control vector (CON255-FLAG), M1-Spastin^{WT}-FLAG, M87-Spastin^{WT}-FLAG, M1-Spastin^{C448Y}-FLAG, M1-Spastin^{S245X}-FLAG as listed in key resource table. The CON255-FLAG plasmid was included as a negative control. After 48 h of induction with doxycycline (5 μg/mL), total protein was extracted using IP lysis buffer (Thermo Fisher Scientific, 87787) supplemented with protease (NCM Biotech, P001) and phosphatase inhibitors (NCM Biotech, P003). For FLAG immunoprecipitation, 500 μL of lysate was incubated with 50 μL of anti-FLAG magnetic agarose beads (Thermo Fisher Scientific, A36797) at room temperature for 20 min with continuous rotation. Beads were then washed three times with PBS to remove nonspecific proteins. Bound complexes were eluted by boiling the beads in 50 μL of 1× SDS loading buffer for 5 min, followed by SDS-PAGE and western blot analysis. For reverse Co-IP, lysates were processed similarly but incubated with RFP-Trap agarose beads (NanoTag Biotechnologies, N0410) to immunoprecipitate mcherry-HDAC6 and examine potential association with spastin isoforms. Eluates were resolved and analyzed by western blotting as described above. Briefly, 5μg input control samples and 15μL IP protein samples were separated using SDS-PAGE and transferred to PVDF membrane. The membrane was blocked at room temperature for 2 h in 5% non-fat dried milk (BioFroxx, 1172GR500) in Tris-buffered saline (TBS, pH 7.4). The samples were then incubated with anti-Flag (1: 2000, Proteintech, 20543-1-AP), anti-Phosphoserine/threonine (1:1000, Amyjet Scientific, PPS-PP2551), anti-HDAC6 (1:1000, Affinity Biosciences, AF6485) or anti-mCherry (1:2000, Abcam, ab205402) at 4°C overnight as listed in key resource table. After washing with TBST (TBS with 0.1% Tween 20), goat anti-Rabbit-IgG (1:2000, Jackson ImmunoResarch Laboratories) or goat anti-chicken-IgG (1:2000, Jackson ImmunoResarch Laboratories) antibodies were applied at room temperature for 2 h. The blot was covered with ECL solution (Tanon, 180–5001) and visualized with Chemiluminescence imaging system (Tanon).

HDAC6 knockdown

HDAC6 siRNA and Con255, M1-C448Y-Flag were transfected into 293T cells, with Con255 serving as the negative control group. After adding 5μg/μL Doxycycline hydrochloride to culture for 48h, total proteins were extracted by using RIPA lysis buffer (Proteintech, PR20035) with protease inhibitor (NCM Biotech, P001) and phosphatase inhibitor (NCM Biotech, P003). 10 μg of protein sample was used for western blotting as aforementioned using anti-Flag (1: 2000; Rabbit; Proteintech; 20543-1-AP),anti-HDAC6 (1:1000; Rabbit;Affinity;AF6485), anti-Acetylated Tubulin (1:1000; Rabbit;Affinity; AF4351) and anti-GAPDH (1:1000; Rabbit, Proteintech; 10494-1-AP).

QUANTIFICATION AND STATISTICAL ANALYSIS

Statistical analysis and data visualization

All control and experimental groups were processed in parallel and analyzed blindly to minimize variability and enhance reproducibility. Data was organized in Microsoft Excel and statistical analysis and graph preparations were carried out using GraphPad Prism version 10. All datasets were subjected to the Shapiro-Wilk's test for normality and outliers were eliminated using the "Identify outliers" program in GraphPad Prism version 10. Statistical comparisons were performed using one-way ANOVA followed by Tukey's post hoc test or unpaired t-tests, with $p < 0.05$ considered statistically significant. Details regarding sample number and statistical analysis can be found in the figure legends and supplementary tables. Figures, graphs, and schematics were assembled using Adobe Photoshop 2024.